Quantifying Sea-Ice Volume Flux using Moored Instrumentation in the Bering Strait

Cynthia S. Travers

A thesis
submitted in partial fulfillment of the
requirements for the degree of

Master of Science

University of Washington

2012

Committee:

Rebecca Woodgate, Chair

Ignatius Rigor

Peter Rhines

Jody Deming

Program Authorized to Offer Degree:

College of the Environment: School of Oceanography

University of Washington

Abstract

Quantifying Sea-Ice Volume Flux using Moored Instrumentation in the Bering Strait

Cynthia S. Travers

Chair of the Supervisory Committee:

Dr. Rebecca Woodgate

School of Oceanography

The Bering Strait is the sole pathway linking the Pacific and Arctic Oceans, and carries one-third of the freshwater entering the Arctic. Although the strait's throughflow dominates the hydrography of the highly productive Chukchi Sea and affects the freshwater budget and thermal structure of the Arctic Ocean, the contribution of sea ice to the freshwater flux has never been satisfactorily quantified. We use data from an array of subsurface moored Acoustic Doppler Current Profilers (ADCPs) and other instruments deployed in the Bering Strait from 2007–2008 to calculate the sea ice and corresponding freshwater volume fluxes through the strait. Data from remote-sensing systems such as the Advanced Microwave Scanning Radiometer (AMSR) and modeled sea level pressure data provide a check of ADCP-derived measurements. We correct the ADCP sea-ice thickness records for instrument-based errors (instrument pitch and roll, ridge shadowing, beam footprint, beam averaging, range outliers) and environment-based errors (sound speed variation, instrument depth, sea-ice freeboard and snow loading), and determine the uncertainty in our volume flux calculations. We estimate the total error in ADCP ice thickness measurements to be of order 0.5 m, with $\sim 46\%$ of this error resulting from beam footprint effects that would remain even if a more precise sonar instrument had been used in our study. We compare our estimates of

sea-ice volume flux (190 ± 50 km^3 yr^{-1}) and corresponding freshwater transport (140 ± 40 km^3 yr^{-1}) through the strait to values from previous surveys, commenting on differences in methodology between the studies. Our findings allow us to assess the utility of subsurface moored ADCPs in quantifying sea-ice presence, thickness, and velocity; the ADCP signal correlation parameter appears to provide a particularly good indication of sea-ice presence. In addition, we consider the use of similar methods to evaluate historical ADCP records and develop a more complete understanding of interannual sea-ice flux variability through the Bering Strait.

TABLE OF CONTENTS

Page

LIST OF FIGURES

LIST OF TABLES

Chapter 1

INTRODUCTION

One-third of the total freshwater input to the Arctic passes through the Bering Strait, the sole pathway linking the Pacific and Arctic Oceans (Aagaard and Carmack, 1989; Woodgate and Aagaard, 2005; Serreze et al., 2006). Although the contribution of sea ice to this freshwater flux has been poorly quantified in the past, measurements of sea-ice thickness and velocity made using moored instrumentation in the strait allow for improved estimates of sea-ice flux. This thesis has two goals: a) to assess the viability of subsurface moored Acoustic Doppler Current Profilers (ADCPs) from Teledyne RD Instruments as a means to estimate sea-ice draft; and b) to quantify the volume flux of sea ice through the Bering Strait using data obtained from an array of these ADCPs and other instruments moored in the strait from 2007–2008. The analysis examines information returned by the ADCPs indicative of sea-ice presence, along-strait velocity, and ice thickness, and aims to correct the ADCP measurements for instrument- and environment-based errors. Comparing the results to sea-ice measurements obtained using other moored and remote-sensing systems enables us to assess the utility of ADCP data in providing sea-ice flux information. A combination of in situ observations and modeled atmospheric parameters allows us to estimate ice flux through the strait. The research literature on observational ice thickness measurement techniques and Bering Strait circulation and transport are reviewed to provide background for the present study.

1.1 Characteristics of the Bering Strait Region

The Bering Strait is bounded to the east by the Seward Peninsula (United States) and to the west by the Chukotka Peninsula (Russia) (Figure 1.1). The strait is relatively narrow

(~ 85 km wide) and shallow (~ 50 m deep) and divided longitudinally into an eastern and western channel by the Diomede Islands. The Bering Strait throughflow has a significant effect on the thermal structure and freshwater budget of the Arctic Ocean (Coachman et al., 1975; Woodgate and Aagaard, 2005; Woodgate et al., 2010). During winter, relatively fresh Pacific waters entering the Arctic form a cold halocline layer, insulating sea ice from the warmer, saline Atlantic water beneath (e.g. Steele et al., 2004). In a global sense, the flux of freshwater through the strait is believed to influence the formation of North Atlantic Deep Water, and thus impact the Atlantic Meridional overturning circulation (e.g. Wadley and Bigg, 2002) and perhaps also the strength of Atlantic western boundary currents (e.g. Huang and Schmitt, 1993).

The annual mean Bering Strait throughflow is ~ 0.8 Sv northward (Roach et al., 1995), but this mean value masks a large amount of variability (Woodgate et al., 2005a). From 1991–1994, Roach et al. (1995) observed that 75% of the variance in moored current measurements in the Bering Strait was aligned with an along-strait axis, which is roughly north-south. Flow magnitude is known to vary on seasonal, weekly, and shorter timescales, with frequent reversals in flow direction (Roach et al., 1995). The hourly measured flow velocity in the narrowest part of the strait ranges from about –50 to 100 cm s^{-1} (typical value ~ 30 cm s^{-1}), where negative values indicate southward flow and positive values signify flow to the north (Woodgate and Aagaard, 2005). Data from three Aanderaa Recording Current Meters (RCMs) show tidal currents in the region to be weak (components generally less than 2 cm s^{-1}), with the tidal flow representing only a small contribution to the flow variability (Woodgate et al., 2005a).

Coachman et al. (1975) identified three principal water masses in the Bering Strait region. Unlike many water masses in the world ocean, which are frequently identified by set temperature and/or salinity (TS) values, Bering Strait water masses show significant interannual variability in TS properties (Coachman et al., 1975). Coachman et al. (1975) described how cold, saline, nutrient-rich Anadyr waters from southwest of the strait dominate the flow in the western channel, while flow in the eastern channel is primarily composed of warmer, fresher, low-nutrient Bering Shelf and Alaskan Coastal waters, also with origins in the south

(Coachman et al., 1975). In addition to the mean flow, two coastal currents are found at times in the strait. The warm, fresh Alaskan Coastal Current (ACC) appears annually in the eastern channel, typically during the summer/autumn months, and can exhibit velocities 50–100 cm s^{-1} stronger than the mid-channel flow (Figure 1.1) (Woodgate and Aagaard, 2005). In the western channel, the cold, fresh Siberian Coastal Current (SCC), which flows southward along the Russian coast, may occasionally reach the Bering Strait (Weingartner et al., 1999).

The northward flow through the Bering Strait dominates the hydrography of the Chukchi Sea (Woodgate et al., 2005a), one of the most biologically productive regions of the world ocean (Walsh et al., 1989; Woodgate et al., 2005b). Within the Chukchi Sea, the Anadyr and Bering Shelf waters merge to form Bering Sea Water (Coachman et al., 1975). The Alaskan Coastal waters tend to follow the Alaskan coastline, although some may spill into the strait under southward wind conditions (Woodgate, R., pers. comm.). Three main pathways (Barrow Canyon, the Central Channel, and Herald Valley) direct outflow from the Chukchi Sea into the Arctic Ocean (Woodgate et al., 2005a). There is also inflow of the SCC from the Arctic through the southern part of Long Strait (Weingartner et al., 1999), which appears to be roughly balanced by a comparable outflow in the northern part of the strait (Woodgate et al., 2005a). Pacific waters exit the Arctic to the North Atlantic Ocean via the Fram Strait or the Canadian Arctic Archipelago (Jones et al., 2003).

A monthly climatology of the Bering Strait compiled from 14 years of mooring data illustrates a strong seasonality in temperature, salinity, and transport properties (Woodgate et al., 2005b). Maximum water temperatures are reached in October, followed by a roughly two-month cooling period that coincides with a near-bottom freshening as the sea surface cools and storms enhance downward mixing of surface waters. Sea ice generally persists in the strait from January to April, while temperatures are at freezing and waters are increasingly saline. The salinity maximum typically occurs around March, at which point the sea ice begins to melt and surface freshening occurs throughout the water column, presumably due to both local and advected ice melt. Highly seasonal Yukon River outflow ($\sim$ 200 km^3 yr^{-1} (Coachman et al., 1975), equivalent to 0.006 Sv if averaged over the year) also influences

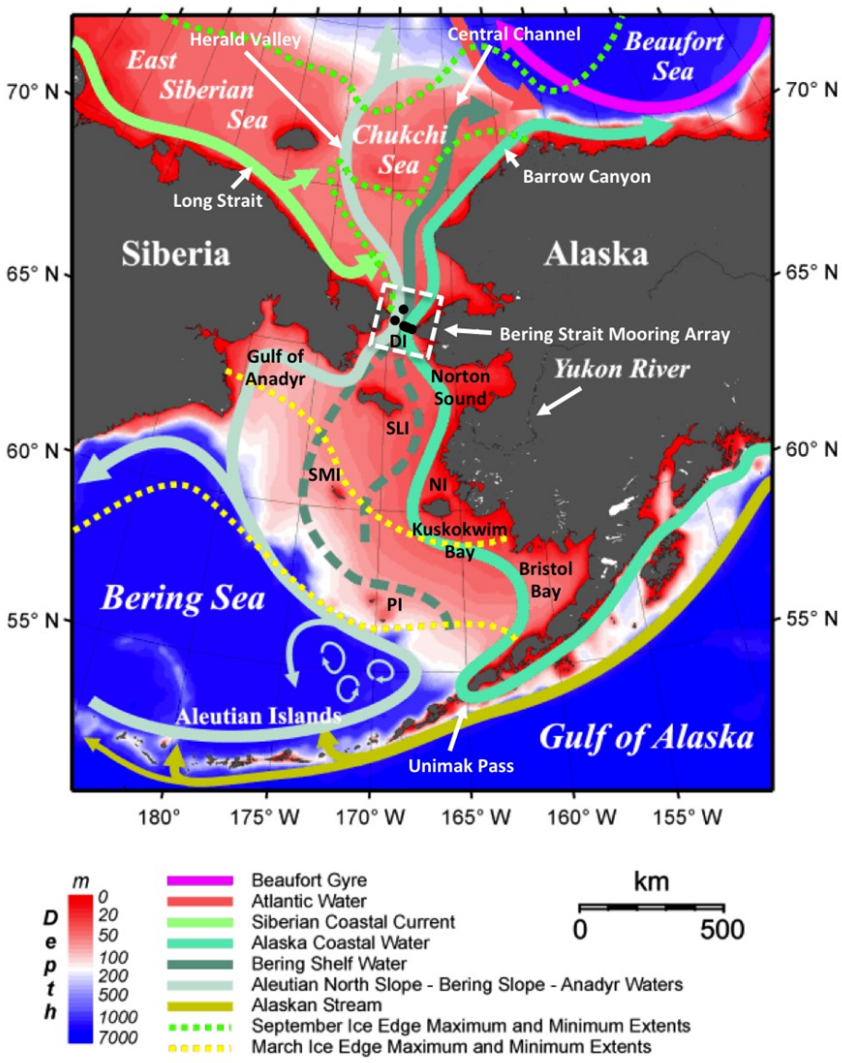

Figure 1.1: Geography and schematic of the mean circulation of the Bering Strait region, indicating major summer water masses and currents, and typical spring and fall ice extents. Black dots inside of the dashed white box show the location of the Bering Strait Mooring Array. Island abbreviations are as follows: DI, Diomede Islands; NI, Nunivak Island; PI, Pribilof Islands; SLI, St. Lawrence Island; SMI, St. Matthew Island (modified from Danielson et al. (2011)).

Bering Strait temperature and salinity, although its arrival time is not yet well documented (Woodgate and Aagaard, 2005). Interannual variability in temperature and salinity is high, and conditions in a particular year may vary widely from the climatology. Overall, the data indicate that the monthly mean temperatures and salinities range between –1.8°C and 2.3°C and between 31.9 psu and 33.0 psu, respectively (Woodgate et al., 2005b). (Throughout this thesis, unless otherwise noted, salinity is measured by the Practical Salinity Scale and noted by use of the dimensionless salinity unit, psu).

Transport through the Bering Strait also varies seasonally, ranging from a climatological winter monthly mean transport of 0.4 Sv–1.3 Sv in the summer months (Woodgate et al., 2005b). The mean transport is largely attributed to a pressure-head slope of order 10^{-6} between the Pacific and Arctic Oceans (Coachman and Aagaard, 1966), combined with local atmospheric effects, most of which appear to be dominated by wind forcing (Aagaard et al., 1985). Following on from earlier studies (Aagaard et al., 1985; Coachman and Aagaard, 1966; Roach et al., 1995), Woodgate et al. (2005a) recreated flow velocities from an empirical linear fit to a local modeled wind field, and determined the pressure-head-driven flow to be about 30 cm s^{-1}. This value exceeded the annual mean flow velocity observed in the same study (25 cm s^{-1}), indicating that the annual mean wind-driven flow opposes the pressure-head-driven flow (Woodgate et al., 2005a). Thus, in general, the northward flow through the strait is weakest in winter, when the southward winds are strongest.

Although the Bering Strait water column is subject to mixing by year-round storms, seasonal surface cooling, and brine rejection, CTD data suggest that typically stratification is strong (water column means are likely 0.5–1 psu fresher and 1–2°C warmer than near-bottom measurements) in the summer and autumn months (Woodgate et al., 2005b). Warm Pacific waters serve as a source of near-surface heat to the Arctic (Woodgate et al., 2006, 2010). The lower density of these Pacific waters (in comparison to Atlantic waters in the Arctic) places them high in the water column over colder, more saline water, creating the potential for enhanced Arctic sea-ice melt (Woodgate et al., 2010).

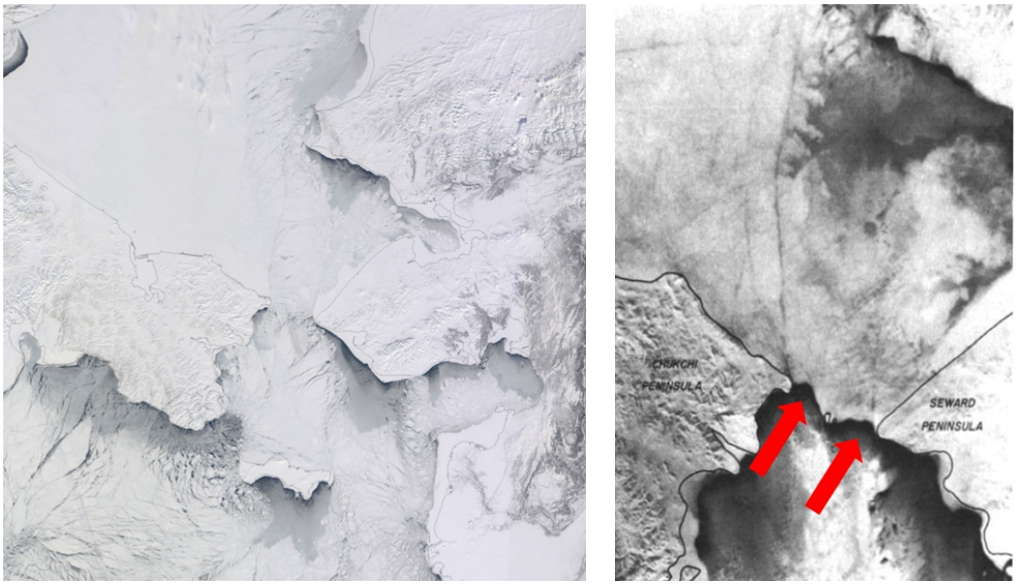

(a) (b)

Figure 1.2: Terra image (a) of the Bering Strait region taken 18 March 2009, showing extent of winter sea-ice cover. Advanced Very High Resolution Radiometer (AVHRR) image from the National Oceanic and Atmospheric Administration (NOAA) (b) for 20 March 1979, with red arrows indicating presence of double arch in sea ice (modified from Torgerson and Stringer (1985)).

1.2 Satellite-Based Sea-Ice Measurements

Sea ice forms annually across much of the Bering Strait from roughly January to April (Figure 1.2(a)), however the ice extent, thickness, and patterns of formation have changed significantly in recent decades. In the 1970s and 1980s, satellite imagery revealed the intermittent presence of double-arched ice formations across the strait between February and May, which effectively prevented the transport of ice through the strait (Figure 1.2(b)) (Torgerson and Stringer, 1985). With increased thinning and retreat of Arctic sea ice observed in satellite measurements since at least 1979, these double arches no longer persist in the present-day Bering Strait (Serreze et al., 2007).

The Bering Strait lies between two different ice regimes – that of the Arctic, and that of the Bering Sea. As evidenced by data from the National Snow and Ice Data Center (NSIDC),

the observed reductions in Arctic sea-ice extent have been most pronounced in September (the typical end of summer ice melt), when the Chukchi and Bering Seas and Bering Strait are ice-free (Figures 1.3(a), 1.3(b)). Within the last decade, satellite measurements of Arctic summer ice thickness have fallen more sharply than those for winter ice thickness (Figure 1.3(c)) (Kwok and Rothrock, 2009). The trends of reduced sea-ice cover and thickness observed in the Arctic are not mirrored in the Bering Sea – the observed Bering Sea ice extent for January 2012 was approximately 104,600 km^2 above the 1979–2000 average of 457,400 km^2, even as the mean Arctic ice extent for January 2012 fell to 1.10 million square kilometers below the 1979–2000 mean (National Snow and Ice Data Center, 2012).

While recent advances (e.g. Laxon et al., 2003) have enabled the remote measurement of sea-ice freeboard (defined as the vertical distance between the air-snow or air-ice interface and the local sea surface (Kwok and Cunningham, 2008)), satellite systems have a limited ability to measure full sea-ice thickness (Kwok and Rothrock, 2009; Kwok et al., 2012). Present-day space-borne sensors can measure radiation emitted or scattered by only the top few tens of centimeters of sea-ice volume; in addition, the sensors are only able to infer the depth of ice keels (downward projecting ridges on the underside of the ice canopy) from measurements of surface ice ridges (Bowditch, 2002; Kwok and Cunningham, 2008). Furthermore, for our purposes, the gridded 12.5-km resolution of satellite Advanced Microwave Scanning Radiometer (AMSR) ice concentration data, made available by the NSIDC, is coarse in comparison to the $\sim$ 85-km width of the Bering Strait. As a result, inclusion of land from the nearby coasts and from the Diomede Islands in the 12.5 by 12.5 km gridboxes can contaminate the ice concentration signal in the relatively narrow eastern and western channels of the strait. In situ ice thickness measurements obtained from moored instruments are thus needed to ground-truth and complement satellite observations of sea ice.

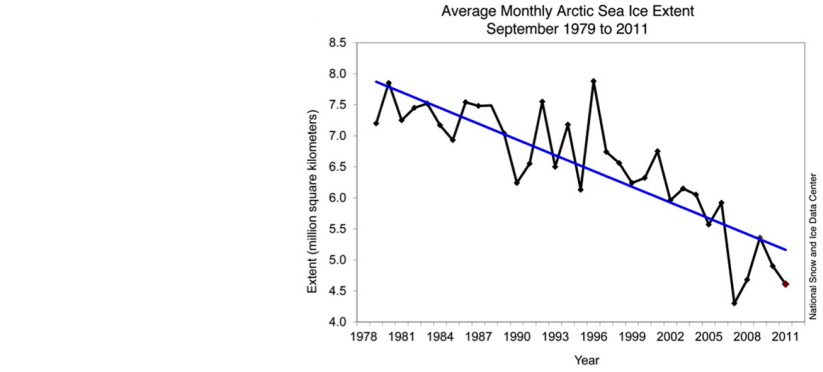

(a)

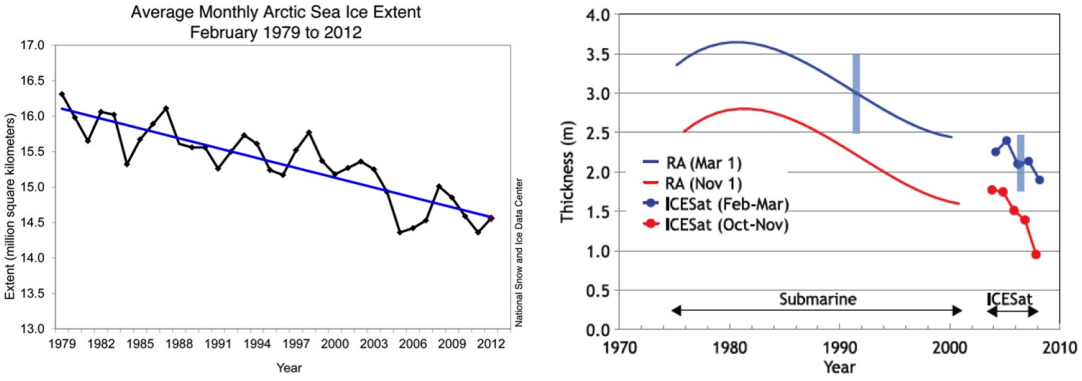

(b) (c)

Figure 1.3: Mean monthly Arctic sea-ice extent for late summer, September 1979–2011 (a) and mid-winter, February 1979–2012 (b) (from NSIDC http://nsidc.org/ arcticseaicenews/, accessed May 2012). Interannual changes in Arctic winter (blue) and summer (red) ice thickness (c) from submarine (RA) and satellite (ICESat) measurements (reproduced from Kwok and Rothrock (2009)).

1.3 In Situ Sea-Ice Measurements

Making in situ measurements of sea ice in the Bering Strait requires the use of moored instruments capable of surviving extended deployments and (preferably) withstanding collisions with deep ice keels. Without the use of an icebreaking vessel, moorings can typically be deployed and recovered only during the summer months, when the likelihood of encountering sea ice is low to zero. A determination of instrument battery endurance for the necessary yearlong deployment is thus critical to successfully recording full datasets. In winter, ice keels may snag instruments positioned too close to the sea surface. Consideration must therefore be given to the instrument depth at which desired measurements can be made with minimal risk of equipment damage or loss due to sea ice.

Instruments that measure the range to objects/surfaces through the emission and detection of acoustic energy, such as Upward Looking Sonars (ULSs) and Acoustic Doppler Current Profilers (ADCPs), provide a viable means by which to measure year-round sea-ice thickness. While our study uses ADCPs to infer sea-ice thickness, it is informative to also consider the more established technology of the ULS, particularly the instrument built by the Applied Physics Laboratory of the University of Washington (the APL-ULS), which has been deployed intermittently in the Bering Strait between 1992 and 2007 (Moritz, D., pers. comm.).

A ULS focuses acoustic energy into a pulse, and measures the time required for the pulse to travel to and from a target. A set detection threshold allows the instrument to identify air-water and ice-water interfaces, but disregards effects such as echoes from phytoplankton blooms (Drucker et al., 2003).

Drucker et al. (2003) used two APL-ULSs in the Bering Sea to observe sea-ice thickness in the vicinity of St. Lawrence Island in the winter of 1999. These ULSs took low-resolution samples at 5-min intervals, and recorded twice-daily high-resolution measurements at 10-s intervals for a period of 25 min. The intermittent high-resolution samples resolved individual features of sea-ice keels as they drifted over the moorings (Drucker et al., 2003), and we will

use similar information from unpublished Bering Strait APL-ULS data in our analysis.

Although ULSs are able to generate detailed profiles of sea-ice bottom topography, they do not measure velocity, which must be quantified to estimate ice volume flux. We therefore investigate the use of ADCPs, which provide both ice velocity data and some measurement of ice draft, in assessing sea-ice flux variability.

Belliveau et al. (1990) described one of the first surveys using moored upward-looking ADCPs to measure sea-ice motion. When fixed to the ocean bottom in ice survey applications, these instruments use high-frequency acoustic backscatter and apply the Doppler Shift principle to measure current velocity (in addition to other characteristics) (Teledyne RD Instruments, 2011). In the Belliveau et al. study, two upward-looking ADCPs (154 and 1228 kHz) were deployed in the Gulf of St. Lawrence (near the Canadian province of New Brunswick). Both instruments sampled in bottom-track mode, an ADCP feature developed primarily to measure the velocity relative to the seafloor of a downward-looking instrument mounted to the underside of a ship (Belliveau et al., 1990; Bowditch, 2002; Teledyne RD Instruments, 2011). In an upward-looking orientation on subsurface moorings, the ADCPs successfully measured sea-ice drift velocity in the bottom-track mode, and the surface velocity and error velocity data provided an indication of when sea ice was present (Belliveau et al., 1990).

Visbeck and Fischer (1995) also recognized the capability of upward-looking ADCPs to detect sea ice during a deployment in the Greenland Sea. In contrast to Belliveau et al. (1990), this study used the ADCP water-track mode, which generates a binned profile of current velocity through the water column (Teledyne RD Instruments, 2011). To determine when sea ice was present, the authors used the water-track target strength and filtered vertical and error velocity variance to define thresholds distinguishing between ice-free and ice-covered periods, which were found to be in good agreement with daily AMSR ice concentration data (Visbeck and Fischer, 1995). In assessing whether water-track data could accurately describe sea-ice velocity, Visbeck and Fischer (1995) concluded that water-track velocity data from the near-surface bin represented sea-ice drift equally well to the bottom-track data used by Belliveau et al. (1990). Although the authors commented on the potential

use of ice thickness and drift measurements to quantify freshwater transport due to sea ice, estimates of ice thickness were not attempted due to a lack of precise pressure measurements at depth (Visbeck and Fischer, 1995).

Melling et al. (1995) revisited Beaufort Sea work from the late 1970s and early 1980s by using two bottom-tracking ADCPs in conjunction with an Ice-Profiling Sonar (IPS) designed to measure precise ranges to the ice-water interface. The ADCPs served to track the motion of sea ice, while the IPS, working similarly to the ULSs previously discussed, generated high-resolution measurements of sea-ice draft. In assessing instrument calibration and error corrections, the authors commented on the effects of sound speed variations, noting that calculations of Doppler velocity made using a constant sound speed based on local conditions were in error by less than 0.5% (Melling et al., 1995). Melling et al. (1995) concluded that simultaneous operation of the IPS and ADCPs could provide detailed observations of sea-ice bottom topography.

Building on the earlier work of Visbeck and Fischer (1995), Shcherbina et al. (2005) obtained concurrent ADCP range and bottom pressure measurements on the Okhotsk Sea shelf from September 1999 to June 2000. Two bottom-mounted ADCPs were deployed at depths of 109 and 144 m, sampling in both bottom-track and water-track modes. Whereas Belliveau et al. (1990) found ADCP surface and error velocities to be strong indicators of sea-ice presence, Shcherbina et al. (2005) observed that high ADCP surface signal correlation values appeared to coincide with increased ice cover. The study addressed a number of potential sources of error in using ADCPs as sea-ice draft profilers, including: atmospheric pressure changes, sound speed variations (also described by Melling et al. (1995), and instrument tilt. Interestingly, the authors found the quality of ADCP water-track and bottom-track ice thickness measurements to be comparable, and concluded that the bottom-track mode is unnecessary for ice profiling (Shcherbina et al., 2005).

Although early efforts to measure sea-ice parameters with ADCPs were focused largely in the Arctic, the instruments have also been used to survey Antarctic sea ice. As part of the Southern Ocean Global Ocean Ecosystems Dynamics (SO GLOBEC) field program, a

subsurface moored ADCP operating in water-track mode was deployed at 108 m at the mouth of Marguerite Bay (Antarctica) from February 2002 to February 2003 (Hyatt et al., 2008). Ice thickness data obtained from the ADCP were corrected for the effects of sound speed variability and instrument tilt, as well as for the footprint error described by Vinje et al. (1998) and discussed in Chapter 2 of this thesis. Hyatt et al. (2008) found the ADCP surface signal correlation parameter, used previously by Shcherbina et al. (2005), to be a poor indicator of sea-ice presence. Instead, Hyatt et al. (2008) used the windowed variances of vertical velocity, vertical error velocity, and surface horizontal speed to detect sea ice.

In summary, although several past studies have used ADCP data to assess sea-ice thickness, surprisingly few (if any) recent studies estimate ice thickness using this technology.

1.4 Freshwater Flux From Sea Ice

In addition to quantifying sea-ice volume flux through the Being Strait using ADCP data, we calculate the freshwater flux due to sea ice through the strait and evaluate our result in light of previous estimates (Aagaard and Carmack, 1989; Woodgate and Aagaard, 2005).

Sea ice is fresher than the seawater from which it forms (typically 4–10 psu for first-year ice) (Kovacs, 1996). Two thirds or more of the salt in seawater is initially rejected during ice formation, while much of the remaining salt is released into the water column over time (Maykut, 1985). If the relatively fresh sea ice is then exported from its formation region, or if the brine injected into the water column is exported, the freezing and melting cycle behaves as an oceanic analog to the atmosphere's hydrologic cycle (Aagaard and Carmack, 1989; Aagaard and Woodgate, 2001). Salinity variations caused by sea-ice formation and melt, along with those resulting from the input of fresh river water and run-off, dominate stratification in the Arctic Ocean and affect vertical circulation (Aagaard and Carmack, 1989).

Aagaard and Carmack (1989) estimated the liquid freshwater flux through the Bering Strait to be 1670 km^3 yr^{-1} (relative to a mean Arctic salinity of 34.8 psu), assuming a mean annual transport of 0.8 Sv and long-term mean salinity of 32.5 psu (Coachman et al., 1975).

This volume represents approximately one-third of the total freshwater input to the Arctic (Aagaard and Carmack, 1989; Serreze et al., 2006), but does not include the contribution of Bering Strait sea ice to the freshwater flux – citing an estimated Bering Strait sea-ice flux of 30 km^3 yr^{-1} and associated annual freshwater inflow of 24 km^3, Aagaard and Carmack (1989) concluded that the import of sea ice through the strait was negligible to the Arctic freshwater budget.

Using moored instrument measurements and ship-based observations, Woodgate and Aagaard (2005) showed that the 1989 calculation of Bering Strait freshwater flux into the Arctic Ocean was a substantial underestimate, mostly due to stratification and input from the ACC, and revised the previous estimate of 1670 km^3 yr^{-1} to 2500 $\pm$ 300 km^3 yr^{-1}. Using simplistic assumptions and data from an ADCP moored north of the Bering Strait for 1990–1991 measuring sea-ice thickness and velocity, Woodgate and Aagaard (2005) estimated an annual mean northward sea-ice transport of 130 $\pm$ 90 km^3 yr^{-1}. Assuming a sea-ice salinity of 7 psu (the same value used in the 1989 calculations), this volume represents a freshwater transport of order 100 $\pm$ 70 km^3 yr^{-1}, a significant change from the 24 km^3 yr^{-1} freshwater flux described by Aagaard and Carmack (1989), but an estimate with very substantial error bars (Woodgate and Aagaard, 2005).

The primary purposes of this study are to evaluate the utility of subsurface moored ADCPs in estimating sea-ice draft, and to quantify sea-ice volume flux through the Bering Strait using data from an array of moored ADCPs and other instruments deployed in the strait for 2007–2008. In describing instrument- and environment-based errors affecting ADCP measurements of ice thickness, we address some limitations of ADCPs in providing sea-ice flux information. We compare our final estimates of sea-ice volume flux and corresponding freshwater flux through the strait to previous flux estimates, and comment on the potential to estimate past Bering Strait sea-ice fluxes using historical ADCP records.

Chapter 2

ANALYSIS OF MOORED ADCP DATA

In this chapter, we describe the location and instrumentation of the eight-mooring array deployed in the Bering Strait from August 2007 to October 2008, with emphasis on the utility of the Teledyne RD Instruments Workhorse Sentinel ADCP. We introduce additional sources of data needed to ground-truth or as input to our calculations of sea-ice properties, including AMSR ice concentration measurements, ULS-measured ice thickness profiles, and numerical weather prediction (from the National Centers for Environmental Prediction, NCEP) reanalysis modeled surface pressure data. The ADCP-measured parameters used to determine sea-ice presence, along-strait velocity, and ice thickness in the Bering Strait are defined, and instrument- and environment-based errors affecting ADCP measurements are discussed. When possible, we adjust the raw ADCP range measurements to account for these errors and improve overall estimates of sea-ice thickness, which will be used in Chapter 3 to estimate sea-ice volume flux.

2.1 Mooring Array Location and Instrumentation

Year-round near-bottom oceanographic moorings have been deployed in the Bering Strait almost continuously since 1990, generally with one mooring at a mid-strait site north of the Diomede Islands (A3) and additional moorings (A1s, A2s, A4s) installed in the eastern and western channels (e.g. Woodgate et al., 2010) (Figure 2.1). Until 2007, at most five moorings (and typically one to three moorings) were deployed each year in the strait region. Deployment of the Bering Strait moorings in 2007 was a joint venture supported by the National Oceanic and Atmospheric Administration (NOAA) RUSALCA (Russian-American Long-term Census of the Arctic) program and the National Science Foundation's Office

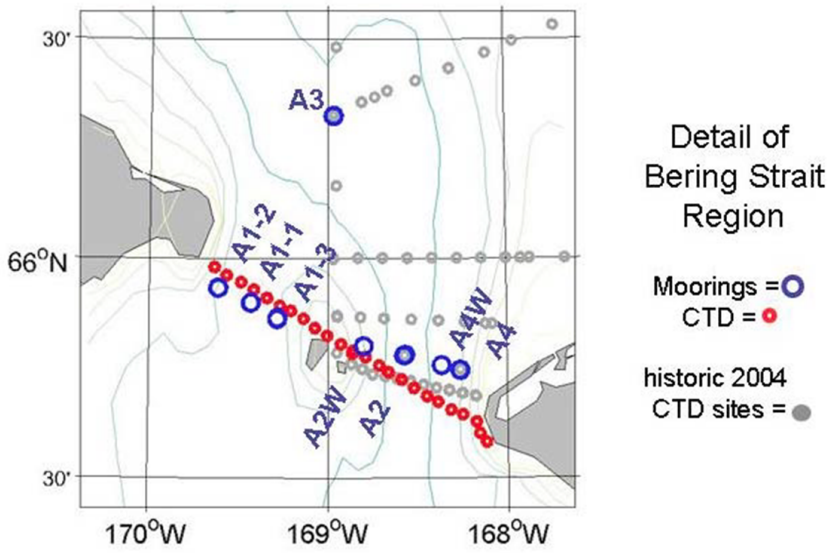

Figure 2.1: Arrangement of moorings in the 2007 Bering Strait array (blue circles). Small red circles indicate locations of CTD sites in 2007, while small gray circles designate CTD sites surveyed in 2004. Irregular gray curves are 10-m bathymetry contours from IBCAO (International Bathymetric Chart of the Arctic Ocean). (Figure taken from Woodgate et al. (2008).)

of Polar Programs (NSF-OPP) International Polar Year program (for more details, see Woodgate et al., 2010).

From August 2007 to October 2008, the Bering Strait array consisted of eight moorings, representing the highest-resolution array ever deployed across the strait (Figure 2.1). Three moorings were deployed across the western (Russian) channel of the strait (from west to east – A1-2-07, A1-1-07, A1-3-07). Four additional moorings were deployed across the eastern (U.S.) channel of the strait (from west to east – A2W-07, A2-07, A4W-07, A4-07) (Woodgate et al., 2008). A final mooring (A3-07) was installed approximately 35 nm north of the strait as a "climate site," intended to provide an average of the flow characteristics through both channels (Woodgate et al., 2007). The last two digits of the mooring name indicate the year of deployment, while the first two characters indicate the mooring location. Moorings A1-1, A2, and A3 are long-term sites, originally established in 1990. Mooring

A4, established in 2001, was placed approximately 7 km off the Alaskan coast, with the expectation that it would record seasonal flow characteristics of the ACC (Woodgate and Aagaard, 2005). Moorings A2W-07 and A4W-07 were new sites added in 2007 to capture across-strait variability.

All 2007 Bering Strait moorings measured water velocity, temperature, and salinity characteristics $\sim$ 10 m above the seafloor using one of two conductivity and temperature recorders (the SBE model 16 SEACAT or SBE model 37 MicroCAT) built by Sea-Bird Electronics (SBE). Six of the eight moorings carried an upward-looking Teledyne RD Instruments 300-kHz Acoustic Doppler Current Profiler (ADCP), as well as a near-surface ISCAT (an SBE 37 MicroCAT in a trawl-resistant housing designed to survive impacts with ice keels) (Woodgate et al., 2008). The sole ADCP deployed in the western channel (at mooring A1-1-07) failed to return any viable data. Moorings at the edges of the eastern channel (A2W-07 and A4-07) were equipped with SBE 26plus SEAGAUGE Wave and Tide Recorders, which served as bottom pressure gauges (BPGs). One mooring in each channel (A2-07 in the east, A1-2-07 in the west) carried In Situ Ultraviolet Spectrophotometer (ISUS) nitrate sensors and optical sensors to measure fluorescence and turbidity (Woodgate et al., 2008) (Table 2.1).

Table 2.1: Instruments Deployed (by Mooring) in 2007 Bering Strait Array. Measured variable abbreviations are as follows: temp, temperature; press, pressure; cond, conductivity; salt, salinity; fluores, fluorescence; transmiss, transmissivity; atten, attenuation; PAR, photosynthetically active radiation. See text for instrument descriptions.

Mooring (W to E, S to N)	Instruments	S/N	Instrument Depth (m)	Water Depth (m)	Measured Variables
A1-2-07	SBE16 w/ optic	4112	39	54	temp, cond, salt, fluores, transmiss, atten
A1-1-07	ISCAT	5432	15	51	press, temp, cond, salt
	ADCP	7924	44	51	N/A
	SBE37 MicroCAT	5361	45	51	press, temp, cond, salt
A1-3-07	SBE37 MicroCAT	4836	36	49	press, temp, cond, salt
A2W-07	ISCAT	5429	17	52	press, temp, cond, salt
	ADCP	2232	44	52	various
	SBE16 SEACAT	0005	47	52	press, temp, cond, salt
	SBE26p-BPG	1134	51	52	press, temp
A2-07	ISCAT	5428	15	55	press, temp, cond, salt
	ADCP	9396	43	55	various
	SBE16 w/ optic	1559	47	55	temp, cond, salt, fluores, transmiss, atten, PAR
A4W-07	ISCAT	5430	16	54	press, temp, cond, salt
	ADCP	9397	44	54	various
	SBE16 SEACAT	0007	47	54	press, temp, cond, salt
A4-07	ISCAT	5431	15	48	press, temp, cond, salt
	ADCP	2270	39	48	various
	SBE16 SEACAT	1698	42	48	press, temp, cond, salt
	SBE26p-BPG	1135	47	48	press, temp
A3-07	ISCAT	5427	12	56	press, temp, cond, salt
	ADCP	0622	45	56	various
	SBE37 MicroCAT	4835	47	56	press, temp, cond, salt

2.2 Teledyne RD Instruments Workhorse ADCP Operating Principles

The ADCPs used in this study are Teledyne RD Instruments 300-kHz broadband Workhorse Sentinel ADCPs running CPU firmware versions 16.20 (A2W-07 and A4-07), 16.28 (A2-07 and A4W-07), and 8.21 (A3-07). Each ADCP is equipped with four transducer faces

arranged symmetrically on the convex transducer head and mounted at an angle of 20° from the vertical axis of the instrument. Data from the ADCP's four sonar beams allow it to calculate three velocity components (e.g., eastward, northward, and vertical), as well as an error velocity component representative of horizontal inhomogeneities in the water velocity (Teledyne RD Instruments, 2011). The beam width of each sonar beam at –3 dB is 2.2°. For this study, both water-track and bottom-track data were recorded half-hourly.

The ADCP's default water-track mode generates a binned profile of current velocity through a water column. With the exception of the ADCP at mooring A3-07, the ADCPs in this study recorded water velocity information from 22 bins, each 2.0 m in length, with a 4.0-m distance from the transducer head to the first bin. The A3-07 ADCP recorded velocity data from 1.0-m bins, however the data were averaged into 2.0-m bins for ease of use. The ADCP's bottom-track mode measures distance to the surface (in the case of our upward-looking ADCPs, this is the ocean surface or the sea-ice bottom) and velocity of the surface relative to the ADCP. The water-track and bottom-track modes use distinct acoustic pulses in their sampling. While water-profiling uses short pulses to obtain high vertical resolution, bottom-tracking requires long pulses to ensonify as much of a surface as possible (Teledyne RD Instruments, 2011). The Bering Strait ADCPs were programmed to emit 115 water-track pulses and 5 bottom-track pulses per 30-min ensemble.

The bottom-track pulses represent an additional draw on the ADCP's limited battery energy, and when compared to the default water-track pulses, have been deemed by some researchers to be redundant (e.g., Visbeck and Fischer, 1995; Shcherbina et al., 2005). As discussed in the previous chapter, Shcherbina et al. (2005) found the quality of ADCP water-track and bottom-track ice thickness measurements to be comparable, concluding that the bottom-track mode is unnecessary for ice profiling. However, quantifying sea-ice volume flux (as we seek to do here) requires not only ice thickness data, but accurate measurements of ice velocity as well. Although the near-surface bins of water-track velocity data can be used to provide sea-ice velocity, we find in our data that the binned data tend to become noisier towards the sea surface. In contrast, the bottom-track mode is designed to measure the motion of an unbroken surface (in most cases, the seafloor), and we find it better

able to track the movement of sea ice. As a result, our analysis of sea-ice characteristics focuses on data obtained through ADCP bottom-track sampling, using RD Instruments' Bottom-Track Mode 4, which, when used with Bottom Resolution Setting 2, estimates the range from the ADCP to the surface with an uncertainty of 1% of the range (Teledyne RD Instruments, 2007).

The Bering Strait ADCPs were deployed in non-vaned frames at the approximate depths listed in Table 2.1. The ADCP uses its internal compass to convert velocity measurements into northward and eastward flow components (Teledyne RD Instruments, 2011). As will be discussed later in this chapter, the Workhorse Sentinel ADCP is equipped with tilt sensors to measure pitch and roll, but current software processing does not adjust range measurements to account for the tilt of the instrument.

2.3 Data Needed to Estimate Sea-Ice Volume Flux

Estimating sea-ice volume flux in the Bering Strait requires data indicative of sea-ice presence, along-strait velocity, and ice thickness. In this section, we identify the ADCP-measured parameters used to determine ice presence and thickness, and describe processing methods needed to extract the desired sea-ice characteristics. We also introduce satellite, in situ, and modeled datasets used to ground-truth our ADCP-based calculations of sea-ice properties.

2.3.1 Ice Presence from Correlation Signal

Previous studies that used ADCPs to measure sea-ice thickness examined a variety of parameters to determine when sea ice was present. In estimating sea-ice thickness in Antarctica's Marguerite Bay using ADCP water-track capabilities, Hyatt et al. (2008) identified five potential ice detection criteria:

– vertical velocity variance,

- error velocity variance,
- horizontal surface speed,
- surface backscatter intensity, and
- surface signal correlation.

Of these five parameters, Hyatt et al. (2008) found that only the first three showed a clear distinction between periods of ice and no ice, as determined using cumulative histograms (Hyatt et al., 2008). Conversely, Shcherbina et al. (2005) examined ADCP data collected in the Okhotsk Sea using both water-track and bottom-track modes, and established surface signal correlation as the most reliable indication of sea ice. The results of our study also suggest that signal correlation is the most useful indicator of sea-ice presence, as outlined below.

Since we seek to detect the presence of ice above the ADCP, each data point must ultimately be interpreted as "ice" or "no ice" to generate a binary time series of ice presence. As suggested by Hyatt et al. (2008), a useful parameter for ice detection is one that has a strong bimodal distribution with two distinct maxima (one for ice, one for open water) identifiable with times when other data suggest the location is ice-covered or ice-free. Once such a criterion is identified, a cut-off value that defines the boundary between the two modes can be defined.

The parameter returned as ADCP correlation is a non-dimensional measure of data quality, and gives "the magnitude of the normalized echo autocorrelation at the lag used for estimating the Doppler phase change" (RD Instruments, 1998). Correlation values range from 0 to 255, with 255 indicating the presence of a solid target, such as an unbroken piece of sea ice. From our datasets, we hypothesize that correlation values significantly less than 255 indicate detection of the air-water interface, which varies continually in shape and does not provide as strong a signal return as sea ice. Zero correlation is an indicator of bad data (RD Instruments, 1998). Thus, we expect high correlation values when sea ice is present.

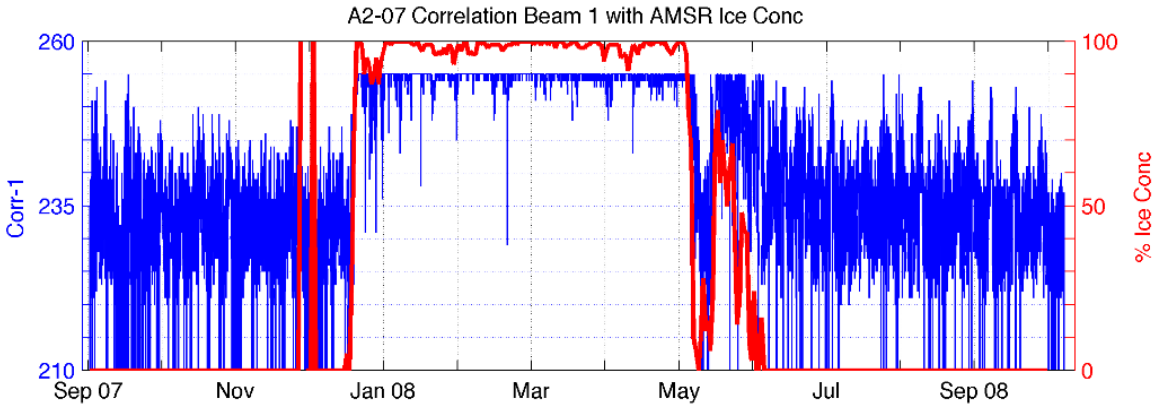

Figure 2.2: Comparison of ADCP Beam 1 correlation at A2-07 (blue) and AMSR percent ice concentration in 12.5 by 12.5 km gridbox located closest to the mooring (red). A correlation value of 255 is the expected return from a solid target, such as sea ice. Note the concurrence of high correlation values and more extensive ice coverage.

To check this, we compare the time series of ADCP correlation values to a time series of 12.5-km resolution gridded AMSR ice concentration data (Figure 2.2). The ADCP signal correlation shows significant variability (with values of 220 to 254) during periods that, according to the satellite data, have little to no sea-ice cover, but ADCP correlation values are remarkably consistent and near to 255 during times of ice cover.

The AMSR ice concentration data serve as an effective quality check for the correlation data, and thus prove useful in identifying an ice/no-ice threshold. To establish a numeric value for this threshold, we plot the correlation signal of each ADCP beam against concurrent AMSR ice concentration data from the nearest AMSR satellite gridbox for each data point in our time series. The AMSR-derived ice concentrations are given at six-hour intervals, and we interpolate these time series onto the half-hourly time-base used by the ADCPs to compare the datasets. The scattered data are divided into two collections: one in which AMSR ice concentration values range from 0 to 50%, referred to here as the lower half, and a second in which ice concentration values exceed 50%, referred to as the upper half (Figure 2.3(a)). The number of data points in each half depends on the amount of time the region experiences less than or more than 50% ice concentration. In the lower half of the data,

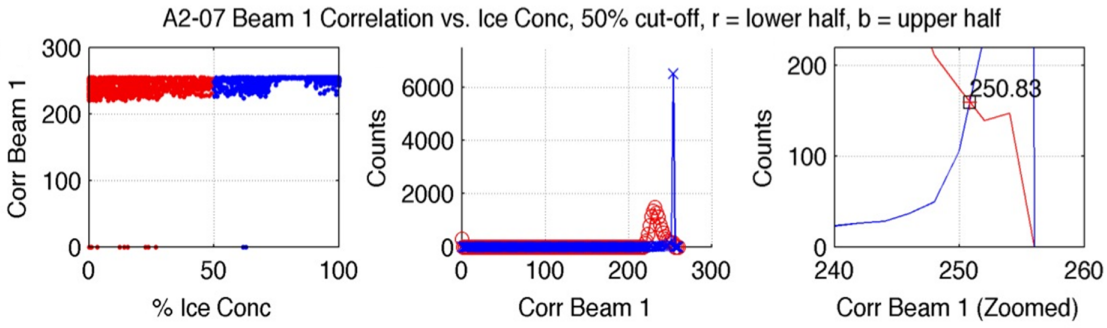

(a) (b) (c)

Figure 2.3: Scatterplot of A2-07 ADCP Beam 1 correlation signal against 12.5-km resolution AMSR percent ice concentration (a), with red points denoting ice concentration values of 0–50% (lower half) and blue points indicating concentration values $> 50\%$ (upper half). Histograms of correlation values (b) for the lower (red) and upper (blue) halves. Labeled intersection point (c) between the two histograms shown in subplot (b).

correlation values of 255 are not anticipated, as sea ice is not expected to be present. In the upper half of the data, which represents time periods when sea ice is thought to be present, the ADCP data are far more likely to include correlation values indicating a solid return.

For each instrument record, a histogram is generated for the ADCP correlation data in each of the upper and lower halves. We plot the two histograms on the same axes, and look for the correlation value at which the curves intersect (Figure 2.3(b)). We take this intersection point to be the ice/no-ice threshold, since above this value more of the data points correspond to ice than to open water (Figure 2.3(c)). In the example of Figure 2.3, the two curves intersect at a correlation value of approximately 251; the intersection points for all ADCPs considered here range from 247 to 253. For each mooring, the threshold values are averaged over all four ADCP beams, and the resultant value is used in subsequent correlation signal filtering for that instrument.

From the mean threshold value, we define (for each instrument) an ice-presence index, which is 1 when correlation values are above the threshold and 0 when values are less than or equal to the threshold. Varying the ice-concentration cut-off value (for example, requiring 80% ice concentration to indicate the presence of sea ice) has little effect on the

corresponding correlation threshold. With a cut-off value of 80% ice concentration, the correlation threshold values have a slightly narrower spread, ranging from 248 to 253.

This processing gives a fairly clear division into ice-covered and ice-free times, however some isolated points remain, which may be ice, or may be outliers in the correlation signal. We thus choose to restrict our definition of ice-covered waters to times when ice is detected consistently over a period of two hours (i.e., at five consecutive sampling points) in the ADCP correlation time series. With a mean flow through the Bering Strait of 30 cm s^{-1}, this corresponds to a continuous length of ice just over 2 km passing above a mooring. Note, however, that such a length of ice may not actually be unbroken over this 2-km distance; it need only be detected as sea ice at the half-hourly intervals recorded by the ADCP. At the same time, this restricted definition of ice-covered waters may cause us to neglect smaller pieces of ice surrounded by open water in our analysis, particularly during the seasonal ice formation observed in mid-late December 2007. If we revisit our earlier ice-concentration cut-off value and require only 20% ice concentration to indicate the presence of sea ice (thereby considering smaller pieces of ice that would be neglected with a higher cut-off value), we obtain a similar range of correlation threshold values (from 245 to 252) to those for the 50% and 80% cut-offs. In addition, AMSR satellite observations suggest that the Bering Strait ice edge advances quickly during seasonal sea-ice formation. For example, AMSR data from mid-December 2007 indicate an increase in sea-ice concentration from 0–10% in both channels to 90–100% coverage across the entire strait over a 3–5-day period. Because we expect these smaller pieces of forming sea ice to be relatively thin, we conclude that the volume flux of sea ice neglected due to our choice of ice-concentration cut-off value is likely small compared to the total sea-ice volume flux over the entire winter season.

2.3.2 Ice Thickness from Range Data

Bottom-track range data measured by an upward-looking ADCP represent the distance from the instrument to the nearest air-water or ice-water interface. Extracting sea-ice thickness from these range data requires numerous corrections, which are discussed at length in the

following sections. After considering the effects of instrument- and environment-based errors on ice thickness measurements, we also address the presence of outlier values that give unrealistic estimates of ice keel depth.

2.3.3 Additional Data Sources

In addition to ADCP and AMSR data, our analysis uses salinity and temperature data from instruments mounted three to four meters below the ADCPs to obtain estimates of density and sound speed through the water. Pressure data from instruments either on the mooring line or located with the mooring anchor allow us to approximate pressure (which is not measured in situ at the ADCPs) and thus derive time series of ADCP depth.

2.4 Instrument- and Environment-Based Range Errors

Obtaining accurate ice thickness measurements from the Bering Strait ADCP range data requires consideration of a series of instrument- and environment-based errors. We define **instrument-based errors** as those stemming from the orientation, design, and/or data processing capabilities of the ADCP. **Environment-based errors** represent instrument limitations resulting from the ADCP deployment location and/or local physical conditions. The errors described in this section are summarized in Table 2.3 at the end of Chapter 2.

2.4.1 Instrument-Based Range Errors

In this section, we examine instrument-based range errors attributed to:

- instrument pitch and roll,
- ridge shadowing,
- beam footprint error,

– beam averaging, and

– range outliers.

2.4.1.1 Instrument Pitch and Roll

Although the ADCP records range, pitch, and roll measurements with every data reading, the value returned as range by the RD Instruments software is corrected only for the slant of the beams from the vertical instrument axis and not for instrument pitch and roll, i.e., the ADCP is assumed to remain upright at all times. This is an invalid assumption for a subsurface moored ADCP, which is free to tilt with flow drag on the mooring. Without correction for instrument pitch and roll, the estimated range error for ADCPs in the Bering Strait array is up to 10 m (Woodgate and Holroyd, 2011). In our study, we thus correct the ADCP ranges for instrument pitch and roll as described by Woodgate and Holroyd (2011). Additionally, we flag as bad data at times when pitch or roll values exceed 15°, since the ADCP's tilt sensor specifications are limited to a range of ± 15° with ± 2° uncertainty (RD Instruments, 1998).

From Woodgate and Holroyd (2011), the angle α_i between each beam of the ADCP and the true vertical V is given by:

$$\begin{aligned}
&\text{Beam1} \quad \cos\alpha_1 = -\sin r \sin\theta + \cos\theta\sqrt{1-\sin^2 r - \sin^2 p} \\
&\text{Beam2} \quad \cos\alpha_2 = +\sin r \sin\theta + \cos\theta\sqrt{1-\sin^2 r - \sin^2 p} \\
&\text{Beam3} \quad \cos\alpha_3 = +\sin p \sin\theta + \cos\theta\sqrt{1-\sin^2 r - \sin^2 p} \\
&\text{Beam4} \quad \cos\alpha_4 = -\sin p \sin\theta + \cos\theta\sqrt{1-\sin^2 r - \sin^2 p}
\end{aligned} \tag{2.1}$$

where p and r indicate instrument-measured pitch and roll, respectively, θ represents the beam angle formed by the axis of each beam and the instrument axis, and the subscript indicates the respective ADCP beam. For the Workhorse Sentinel ADCPs used in this study, θ is 20°. To derive the tilt-corrected ADCP range for each beam from the range data returned by the ADCP, the following equation is used with the relevant values of nominal

beam angle (θ) and beam angle to true vertical (a_i) outlined above:

$$R_{\mathrm{Corr}} = R_{\mathrm{Init}} \frac{\cos a_i}{\cos \theta} \tag{2.2}$$

where R_{Init} denotes ADCP range from the RD Instruments software, and R_{Corr} represents the tilt-corrected range desired. The small angle approximation of this result matches the solution presented by Shcherbina et al. (2005) for deriving the constant instrument tilt of an ADCP mounted on a stable bottom platform. Applying this tilt correction to ADCP range data from the Bering Strait reduces the discrepancy in ranges between beams from up to 10 m to approximately 0.4 m (Woodgate and Holroyd, 2011). The error remaining after correction is comparable to the manufacturer's quoted uncertainty of 1% of the initial ADCP range to the surface in open water using the instrument's Bottom Resolution Setting 2 (Teledyne RD Instruments, 2007).

2.4.1.2 Ridge Shadowing

The effects of ridge shadowing, described by Wadhams (1981) and Vinje et al. (1998), are illustrated in Figure 2.4. When sonar beams are inclined to the vertical, as in the case of an upward-looking ADCP, shadow zones may occur behind steep ice keels. In this situation, the sonar readings overestimate ice thickness, since the deeper ice keels block the sonar measurements of shallower ice features beyond (Wadhams, 1981). The magnitude of this effect depends on the steepness of the underwater ridges in the ice compared to the slope angle of the ADCP beams. Higher resolution ice thickness measurements from older APL-ULS data in the strait allow us to estimate the magnitude of the ridge-shadowing error for our Bering Strait ADCP data.

No ULS instruments were installed in the 2007 Bering Strait mooring array, but data obtained from a 2002 ULS deployment at mooring site A2 provide an approximation of recent sea-ice characteristics in the region. While an ADCP is equipped with four angled sonar beams, the APL-ULS instrument used a single beam directed vertically upwards. The 2° nominal half-power beam width of the ULS is close to the ADCP beam width of 2.2° (Drucker et al., 2003). The ULS operated with a higher temporal sampling resolution

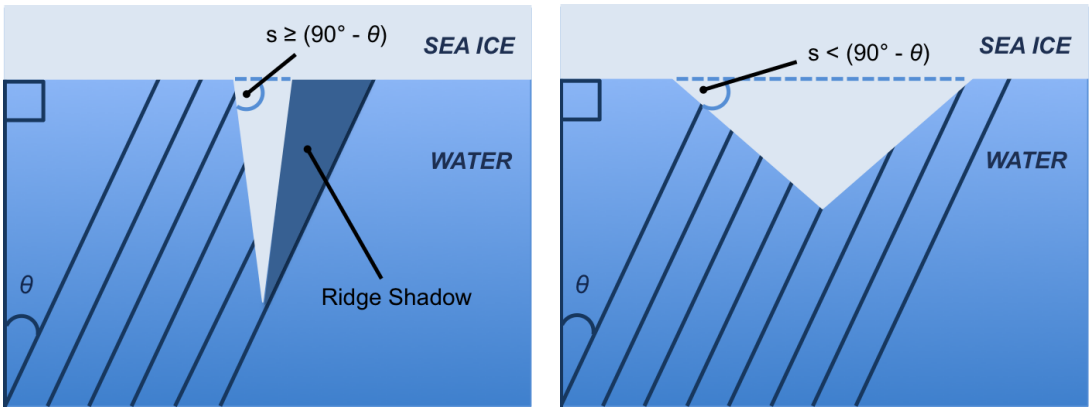

(a) Steep Ice Keel

(b) Shallow Ice Keel

Figure 2.4: Ridge-shadowing effect caused by a steep ice keel (a) and similar diagram of a shallower ice keel (b), which does not generate a ridge shadow. The ridge shadow in (a) results in an overestimate of ice keel thickness. The angle θ represents the ADCP beam angle to the vertical instrument axis. (For the Bering Strait ADCPs, this angle is 20°.) The pale blue color in the diagrams represents sea ice, while the medium-blue color signifies seawater beneath the ice.

than our ADCPs, measuring five readings at an 8.6-s gap, followed by a 17.6-s pause for a period of about 25 min every 12 h (Moritz, D., pers. comm.). Assuming a nominal ice speed of 30 cm s^{-1} (Woodgate et al., 2005b), we estimate that each set of five ULS high-resolution readings sampled the ice at a horizontal spatial resolution of about 2.6 m, while the subsequent pause represented a gap of about 5.3 m. Continuity of the ULS thickness readings during the high-resolution sampling suggests that the 8.6-s data are able to resolve individual ice keels. (In contrast, the A2-07 ADCP sampled sea ice by averaging five bottom-track measurements over a 30-min period. If we again use a mean ice velocity of 30 cm s^{-1}, we calculate a horizontal spatial resolution of 540 m for the ADCP, far coarser than the ULS resolution.)

In describing the steepness of an ice keel, we use the convention that zero slope represents flat ice. An ice keel slope approaching 90° from the horizontal indicates an increasingly vertical protrusion of ice. By geometry, we determine that only ice keels having a slope of 70° (from 90°– θ, where $\theta = 20°$) or greater may be subject to the shadowing error effects,

as seen in Figure 2.4(a). We combine ULS thickness data (Moritz, D., pers. comm.) with ice velocity estimated from the velocity of the underlying water (direct estimates of ice velocity are not available for 2002, so 2002 ice velocity is estimated from 2002 near-bottom water velocity assuming the same correlation of velocity at depth to ice velocity found in the modern ADCP data). In doing so, we establish that 99.7% of the ice keels observed in 2002 had slopes less than 70°. This is in agreement with ice keel studies from elsewhere in the Arctic, which found mean slopes of 33° for newly formed ridges and 24° for weathered ridges (Martin, 2007; Wadhams, 1978). Since the keel slope threshold for shadowing effects is 70° in our case, these lines of evidence indicate that ridge shadowing is not likely to be an issue for our dataset.

2.4.1.3 Beam Footprint

The footprint of an ADCP beam is the elliptical area ensonified by the sonar beam when it reaches the nearest ice surface, and is a function of distance of the ADCP below the ice, and sonar beam width and spread. The bottom-track range most strongly favors the first return from the ensonified area (Strong, B., Teledyne Instruments, pers. comm.). As the first return will originate from the deepest/nearest part of an ice keel within the beam footprint area, an irregular ice surface will cause the ADCP range to be less than the distance between the instrument and the mean draft over the full beam width. This effect, which may result in a systematic overestimation of ice keel draft, is known as footprint error (Vinje et al., 1998). A larger beam footprint results in a greater expected error.

In the data used here, the ADCP beams are at an angle of 20° to the instrument axis, with beam width of 2.2° at –3 dB (Teledyne RD Instruments, 2011). The beam itself is 9 cm in diameter, which is small compared to the 4.0-m spread of the beam over distances of 40–45 m. Using the instrument depths included with mooring deployment records, we estimate that the maximum beam footprint diameters range from 3.4 to 4.0 m, with the surface footprints about 12.5 to 14.5 m away from the mooring site. To quantify the footprint error in our study, we use published estimates of the footprint effect made from ice bottom

topography surveys in the Fram Strait and northern Barents Sea from 1986 to 1989 (Vinje et al., 1998). For a sonar aperture angle of 5° and instrument depth of 50 m, which approximate the set-up of the Bering Strait ADCPs, Vinje et al. (1998) estimated a footprint error of 0.35 m for first-year winter sea ice. Because all sea ice disappears from the Bering Strait in summer, we suspect that first-year ice dominates in the region, and thus estimate footprint errors at the Bering Strait moorings to be of order 0.35 m.

2.4.1.4 Beam Averaging

In measuring range to the nearest interface, the ADCP records the range for each beam as a separate time series. To estimate ice thickness at each mooring location, we average the range values measured by each beam. Variations in the range return among the beams are to be expected due to the irregular nature of the ice surface being ensonified.

In considering the effects of averaging the ADCP range data across all four beams, we must also acknowledge that the process may result in a loss of peaks in the signal. If bottom ice roughness is considerable, one ADCP beam may measure the range to an ice feature not "seen" by the other three beams. We recognize that our processing likely causes smoothing (and therefore underestimation) of the ice keel depths, however taking the mean of the four range measurements still represents our best available approximation of ice keel thickness. Among the ADCPs moored in the eastern channel of the Bering Strait, the standard error in the mean of the four beams for each data point ranges between about 0.2 and 0.35 m. This error due to beam averaging appears to increase with sea-ice thickness, which we calculate in Chapter 3.

2.4.1.5 Range Outliers

After correcting our ADCP range data for smaller-scale instrument-based errors, we seek to remove unrealistic measurements of ice thickness from the data. By establishing upper and lower threshold values based on realistic estimates of ice thickness and sea surface height,

outlier values can be filtered from our time series (Figure 2.5). In our analysis, we use a lower threshold of 20 m below the sea surface (corresponding to a 20-m thick ice keel), and an upper threshold value of 5 m above the sea surface. We choose these cut-off values after subtracting the mean open-water range from the range time series at each mooring to estimate the range variability from the sea surface. Because most Bering Strait sea ice is suspected to be relatively thin first-year ice, we do not expect to see ice keels thicker than our lower threshold value of 20 m (Moritz, D., pers. comm.). As discussed in Section 2.4.2.2, the maximum sea surface height variability due to geostrophy in the strait is approximately 0.2 m, making our upper cut-off value of 5 m a reasonable threshold.

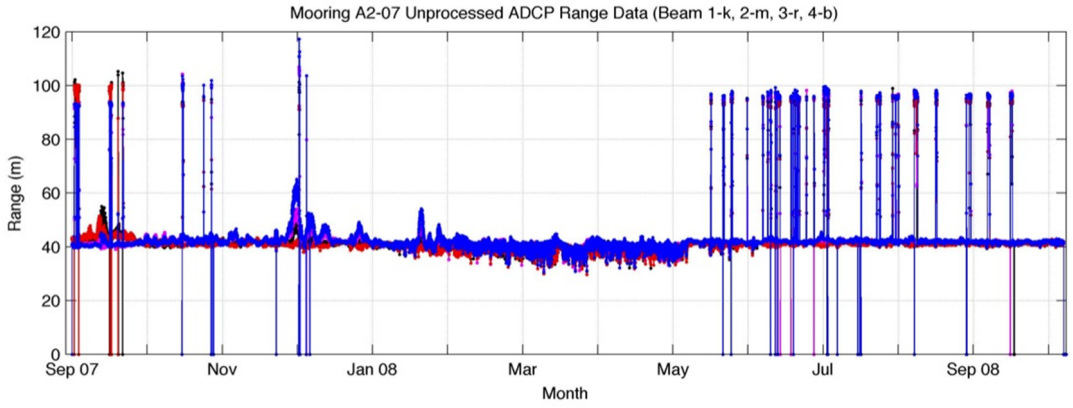

(a)

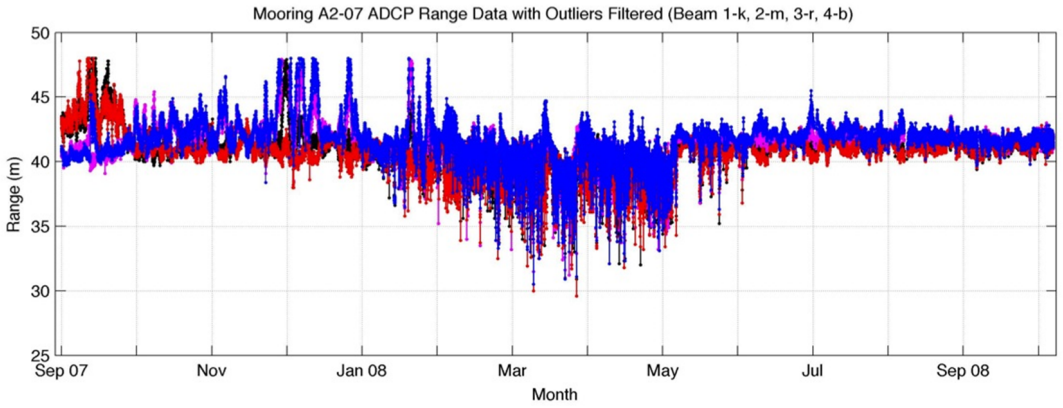

(b)

Figure 2.5: Unprocessed ADCP range time series for mooring A2-07 (a), and time series after filtering of outlier values (b). Ranges for each ADCP beam are plotted separately (Beam 1–black; Beam 2–magenta; Beam 3–red; Beam 4–blue).

2.4.2 Environment-Based Range Errors

In this section, we examine ADCP environment-based range errors attributed to:

– sound speed variation,

– instrument depth below the sea surface, and

– sea-ice freeboard and snow loading.

2.4.2.1 Sound Speed Variation

The speed of sound through seawater, c_s, is calculated from the equation of state as a function of pressure, temperature, and salinity, as expressed by:

$$c_s^2 = \left(\frac{\partial p}{\partial \rho}\right)_{\theta,S} \tag{2.3}$$

where p represents pressure, and ρ represents density as a function of potential temperature, θ, and salinity, S (Gill, 1982). The international standard algorithm to calculate sound speed in seawater, also known as the UNESCO algorithm, results from the work of Chen and Millero (1977) and is used to generate Figures 2.6 and 2.7 below.

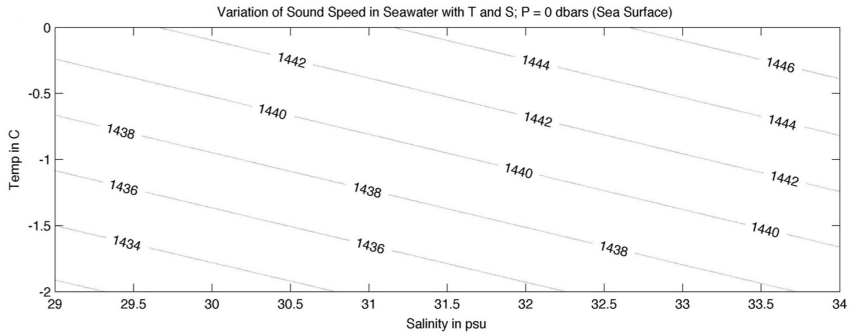

(a)

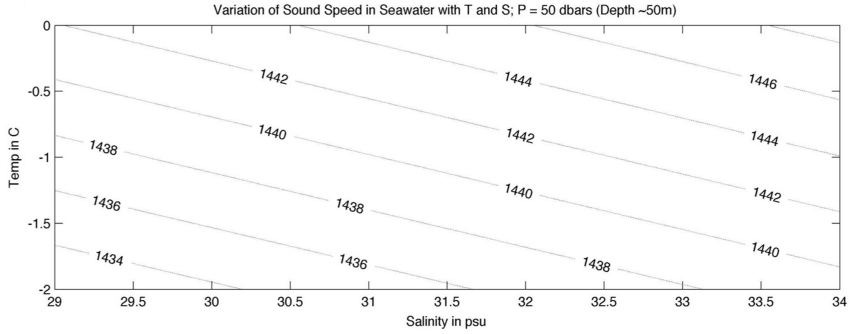

(b)

Figure 2.6: Variation with temperature (T) and salinity (S) of sound speed in seawater, calculated for (a) surface pressure (0 db) and (b) pressure at $\sim$ 50 m depth (50 db). The contours represent lines of constant sound speed in m s^{-1}.

The Bering Strait ADCPs calculated sound speed using in situ temperature measurements and a fixed salinity value of 33 psu. The assumption that salinity remains constant introduces error into the ADCP range measurements, as we see when considering the relationship between sound speed (s_{Actual}), ADCP beam pulse transit time (T), and distance from the ADCP to the ice-water interface (D), viz.

$$D = s_{\text{Actual}} \times \frac{T}{2} \tag{2.4}$$

However, the distance ($D_{\text{Instrument}}$) returned by the ADCP uses the sound speed ($s_{\text{Instrument}}$)

calculated without the change in salinity. We can thus write:

$$D_{\text{Actual}} = \left(\frac{s_{\text{Actual}}}{s_{\text{Instrument}}} \right) \times D_{\text{Instrument}} \tag{2.5}$$

where D_{Actual} represents the distance to sea ice when in situ salinity measurements are considered to calculate the speed of sound.

The axes of Figure 2.7 show the full range of temperature (T) and salinity (S) values observed when sea ice is present in the Bering Strait (from roughly January to April), taken from 14 years (1990–2004) of Bering Strait mooring data. The dashed red boxes indicate the extent of monthly-averaged salinity values for January to April in a 1990–2004 Bering Strait climatology (Woodgate et al., 2005b). Although these values are based on near-bottom readings, comparisons with near-surface ISCAT measurements show the strait to be mostly well mixed in ice-covered times.

Figure 2.7(a) depicts the variation in sound speed with T and S values at the surface, which is also shown in Figure 2.6(a). Subplot (b) of Figure 2.7 illustrates the changes with T and S of the sound speed ratio ($s_{\text{Actual}}/s_{\text{Instrument}}$) given in Equation (2.5) above (i.e., the fractional correction required). For our January–April climatology T and S values, we see that the sound speed ratio is very close to 1.0, indicating that s_{Actual} is only slightly less than $s_{\text{Instrument}}$. Figure 2.7(c) shows the subsequent corrections (in meters) needed to adjust the ADCP range data at a depth of 40 m (the approximate depth at which the 2007 Bering Strait ADCPs were deployed). Although the effect of sound speed variation on our data is small ($\sim$ –0.02 m), it is relatively easy to calculate, and is thus included in our error corrections.

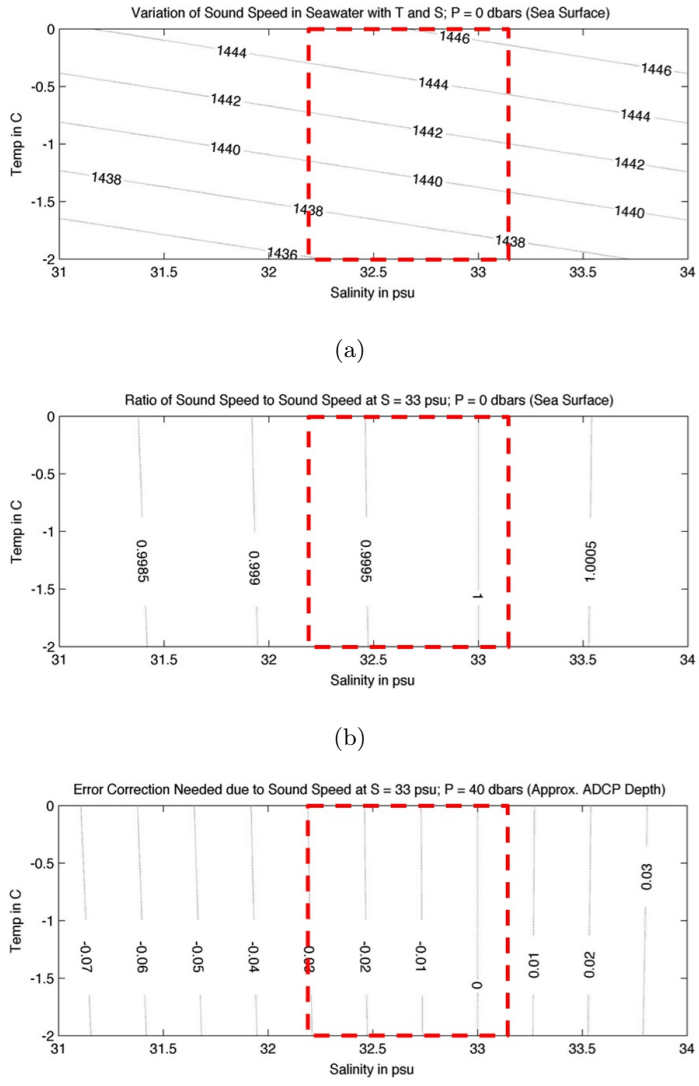

(a)

(b)

(c)

Figure 2.7: Variation with Temperature (T) and salinity (S) of sound speed in seawater, calculated for sea surface pressure (a), ratios of s_{Actual} to $s_{\text{Instrument}}$ at the sea surface (b), and subsequent corrections (in m) needed to adjust range data from the Bering Strait ADCPs deployed at ~ 40 m depth (c). The dashed red boxes indicate the extent of monthly-averaged salinity values for January to April in a 1990–2004 climatology (Woodgate et al., 2005b).

2.4.2.2 Instrument Depth Below the Water Surface

To convert ADCP range data into sea-ice thickness measurements, we need to know the depth of the ADCP below the sea surface at all times. As depicted in Figure 2.8, the depth of sea ice below the surface, D_{I}, can be expressed as follows:

$$D_{\mathrm{I}} = D_{\mathrm{C}} - R \tag{2.6}$$

where D_{C} represents the depth of the ADCP below the water surface, and R is the range to sea ice measured by the ADCP.

Several issues complicate our determination of ADCP depth. Sea surface height in the Bering Strait, which affects pressure (and, therefore, estimated depth) at mooring instruments, is affected by a number of physical processes driven by ocean and atmosphere interactions. Assuming the geostrophic balance of along-strait flow, v, with across-strait sea surface slope, we can write:

$$fv = g\frac{\partial \eta}{\partial x} \tag{2.7}$$

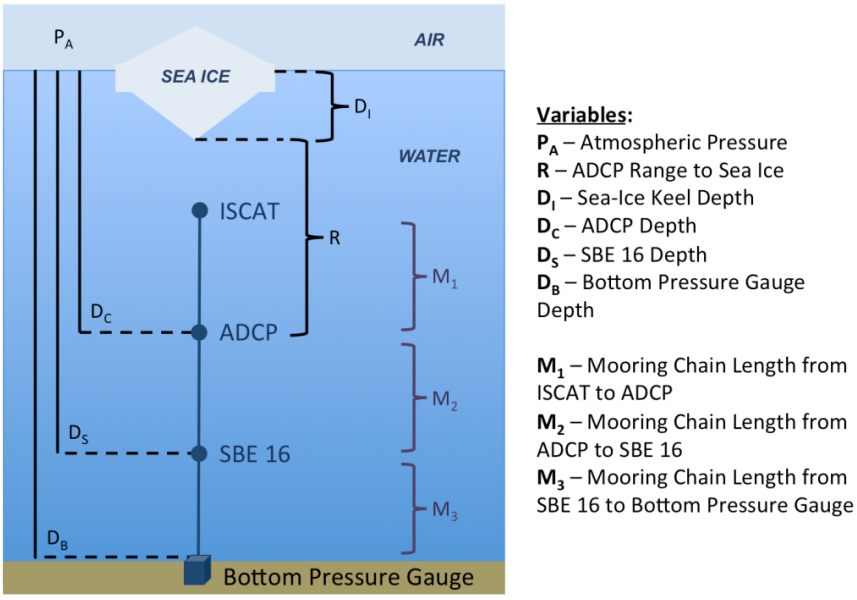

Figure 2.8: Diagram of hypothetical Bering Strait mooring with bottom pressure gauge, SBE 16, ADCP and ISCAT.

where f is the Coriolis parameter, g is acceleration due to gravity, η represents sea surface height, and x indicates the across-strait direction (Gill, 1982). Assuming a transport through the Bering Strait of 1.0 Sv (an approximation of the annual mean northward throughflow of ~ 0.8 Sv), we estimate that sea surface height variability across the strait due to geostrophy is ~ 0.2 m. Performing a similar calculation using an along-strait transport of 3.0 Sv (representing the magnitude of stronger flows on a weekly timescale (Roach et al., 1995)) yields an estimated sea surface height variability of ~ 0.6 m. Thus, currents through the strait have a significant effect on sea surface height, which we are able to account for through pressure sensor measurements.

In contrast, tidal effects on sea surface height in the Bering Strait are minimal, as the magnitude of tidal flow (~ 2 cm s^{-1}) represents only a small contribution to the estimated 30 cm s^{-1} mean current velocity (Woodgate et al., 2005a).

Variations in atmospheric sea level pressure can affect sea surface height as described by the inverse barometer effect (Gill, 1982). However, for our purposes, we subtract variations in atmospheric pressure from in situ pressure readings at depth to extract the pressure variations due to sea level or ocean density changes.

The four ADCPs moored across the eastern channel of the strait were not equipped with pressure sensors, and the depth of each mooring and distances between instruments are not precisely known. Fortunately, three of the four moorings (A4-07, A4W-07, A2W-07) included SBE 16 conductivity and temperature recorders that also measured pressure. In the following section, we use these and other pressure data from bottom pressure gauges (BPGs) at moorings A4-07 and A2W-07 to estimate ADCP depth and determine the severity of mooring pull-down effects. Mooring pull-down describes the condition in which flow drag on a mooring causes the mooring to tilt or heel over, thereby increasing the depths of instruments positioned along the mooring line. Referencing Figure 2.8, we can express the time series of mooring pull-down as:

$$\text{Mooring Pull-Down} = M_3 - (D_\text{B} - D_\text{S}) \tag{2.8}$$

where M_3 is the distance on the mooring line between the BPG and SBE 16, and D_B and

D_S are the respective time series of depths of the BPG and SBE 16 below the water surface as obtained from the instrument pressure records.

2.4.2.2.1 Deriving ADCP Depth from SBE 16 Data

To infer ADCP pressure and depth, we use pressure data from the SBE 16s moored approximately 3 m below the ADCPs at mooring sites A4-07, A4W-07, and A2W-07. (The SBE 16 at mooring A2-07 was not equipped with a pressure sensor.) As illustrated in Figure 2.8, the ADCP depth (D_C) can be determined using the SBE 16 depth (D_S) and the distance between the two instruments on the mooring line (M_2) by using:

$$D_C = D_S - M_2 \tag{2.9}$$

To begin solving for the SBE 16 depth (D_S), we detrend each SBE 16 pressure time series to compensate for instrument drift over time. For each SBE 16, the measured pressure (P_{Sensor}) is equal to the sum of the surface atmospheric pressure (P_A) and the weight of the water column above the instrument, viz.

$$P_{Sensor} = P_A + \rho g H \tag{2.10}$$

where ρ is seawater density, g is acceleration due to gravity (adjusted for latitude), and H is the height of the water column above the instrument. For our calculations we seek to know H, which is equal to the instrument depth, and thus we must subtract atmospheric pressure from the pressure sensor reading. The atmospheric pressure time series used here are NCEP modeled sea level pressure data from the 2.5° latitude by 2.5° longitude NCEP gridbox located closest to each mooring for the relevant time period. (NCEP reanalysis data provided by the NOAA/OAR/ESRL PSD, Boulder, Colorado, USA, from their website at http://www.esrl.noaa.gov/psd/.) We use in situ density calculated from the temperature and salinity data recorded by the SBE 16s. This assumes the water column is well mixed, which, as evidenced by ISCAT data (not shown), is a reasonable assumption during ice-covered periods. Even during the summer months, however, the density stratification is at most 2 kg m^{-3}, yielding an error of less than 0.2% (Woodgate, 2004).

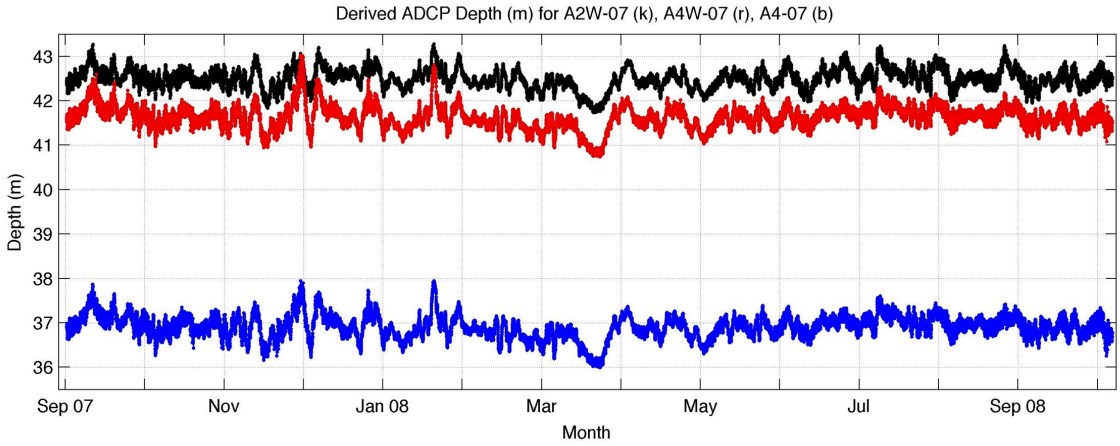

Figure 2.9: Derived ADCP depth time series for moorings A2W-07 (black), A4W-07 (red), and A4-07 (blue).

As noted in Equation (2.9), we need to know the distance between the SBE 16 and ADCP on the mooring line (M_2) to derive ADCP depth at each mooring. Although instrument data files from the 2007 deployment provide the approximate lengths of chain used between instruments, the heights of the instruments and their frames also contribute to the distances M_1, M_2, and M_3, and are not precisely known. To better estimate M_2, we take (at each mooring) the mean of the difference between the ADCP range and SBE 16 depth during open-water periods. By subtracting this value of M_2 ($\sim$ 5.0 m for all three moorings) from the SBE 16 depth time series, we arrive at time series of ADCP depth for moorings A4-07, A4W-07, and A2-07 (Figure 2.9).

Although the eastern channel ADCPs are moored at different depths, it is clear from Figure 2.9 that pressure variability at ADCP depth is strongly correlated across the strait. The variability among these time series results from changes in sea surface height due to waves, mooring pull-down, and density, flow, and atmospheric effects. We expect that many of these effects will show across-strait coherence. As an example, the length scales of atmospheric variability are far greater than the width of the Bering Strait, and we therefore expect similar measurements of sea level pressure at all mooring sites.

The high coherence in ADCP depth observed in Figure 2.9 suggests that differences in density and wave fields across the strait are small. Observations show that the ocean flow field is mostly homogeneous across the strait (away from boundary currents), and thus we might anticipate that sea surface slope is also coherent across the strait. This latter assumption, although simplistic, has been used in previous altimeter work (Cherniawsky et al., 2005). Given the homogeneous flow and similar design of all eastern channel moorings, we also expect similar mooring pull-down measurements at all sites.

2.4.2.2.2 Interpolating ADCP Depth at Mooring A2-07

Due to the lack of an SBE 16 pressure time series at mooring A2-07, we require a different method to estimate ADCP instrument depth at the site. The high coherence in ADCP depth across the strait leads us to test if linear interpolation of SBE 16 pressure data between the neighboring moorings (A4W-07 and A2W-07) is appropriate. Figure 2.10 shows scatterplots of the demeaned, detrended SBE 16 pressure time series at these two moorings. The correlation between the two time series is strong, particularly when we consider only the ice-covered periods when wave effects are expected to be small ($r \approx 0.94$) (Figure 2.10(b)). As we are concerned primarily with ADCP depth while sea ice is present, the results suggest that interpolation of SBE 16 pressure data to the A2-07 mooring site is a reasonable strategy.

We first calculate the mean SBE 16 pressure during periods of open water, and subtract this value from the full pressure time series at moorings A4W-07 and A2W-07 to obtain time series of pressure variability (Figures 2.11(a), 2.11(b)). We then linearly interpolate between the two pressure variability time series, taking into account the distance between the moorings, to derive a time series of pressure variability at the A2-07 SBE 16 (Figure 2.11(c)).

This gives us a time series of estimated pressure variability at A2-07, but not the total pressure. However, we can estimate the required offset (equivalent to the mean depth of the ADCP) by using the open-water range data measured by the A2-07 ADCP. We generate a

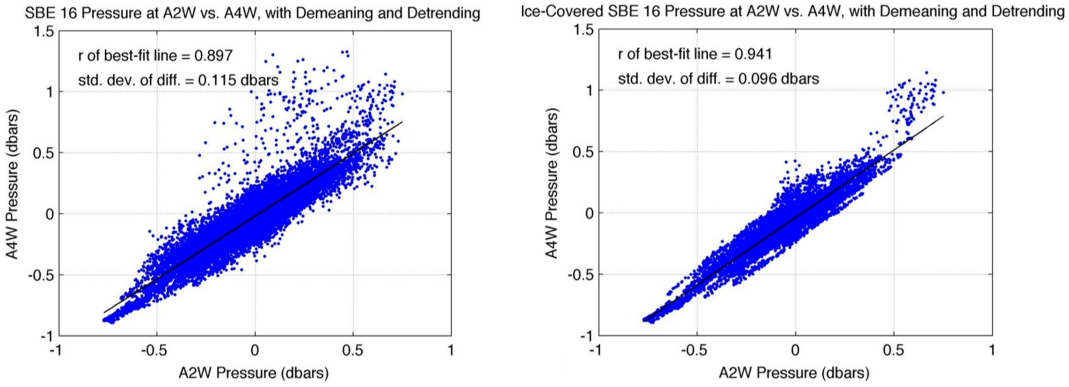

(a) (b)

Figure 2.10: Scatterplots of demeaned, detrended SBE 16 pressure time series at A2W-07 (x-axis) and A4W-07 (y-axis) for the full length of the time series (a) and the for ice-covered period only (b).

scatterplot of the interpolated SBE 16 pressure variability and A2-07 ADCP range during open-water periods, and look for where the best-fit line crosses the y-axis (Figure 2.12). This intercept gives us the offset we require.

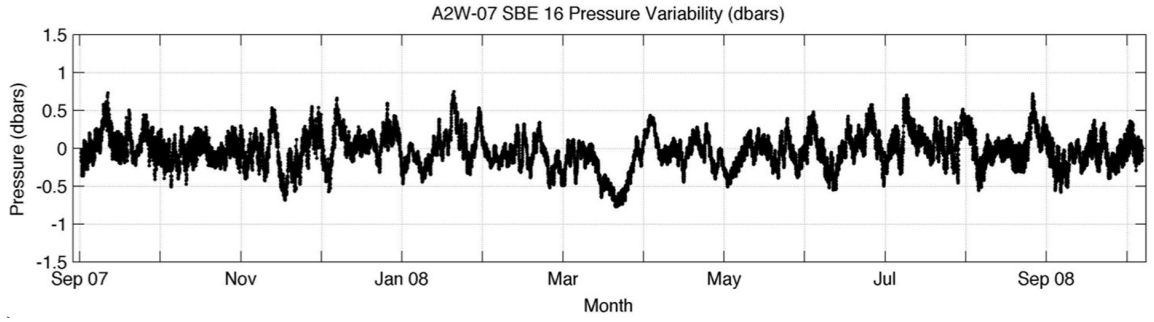

(a)

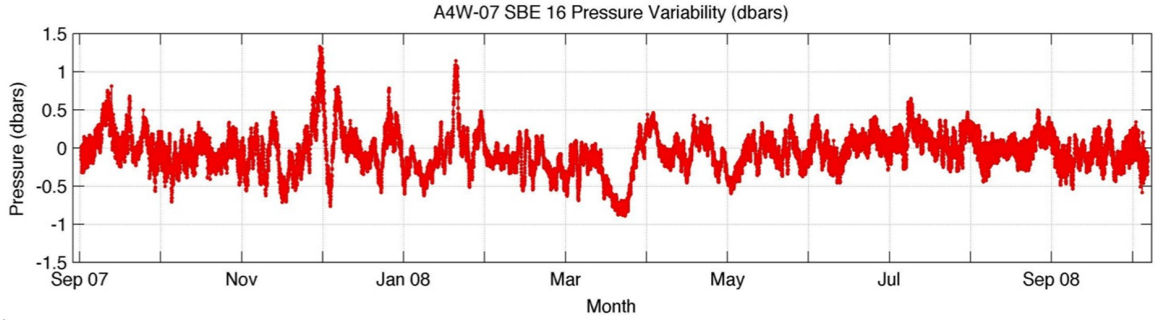

(b)

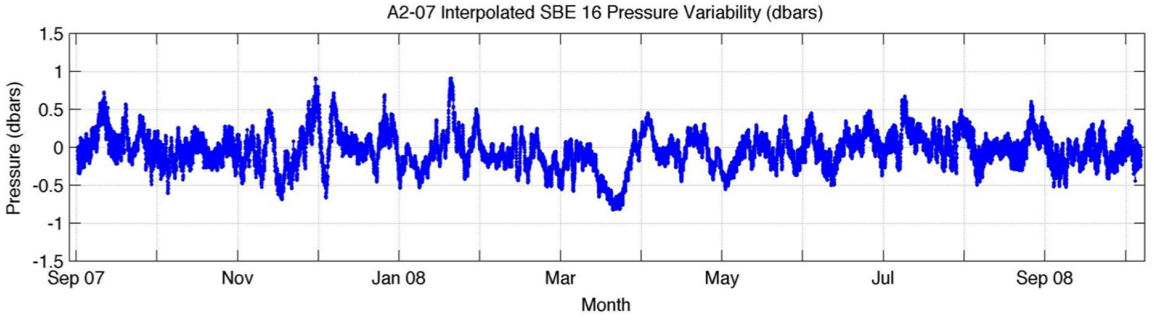

(c)

Figure 2.11: SBE 16 pressure variability for A2W-07 (a), A4W-07 (b), and interpolated pressure variability for A2-07 (c).

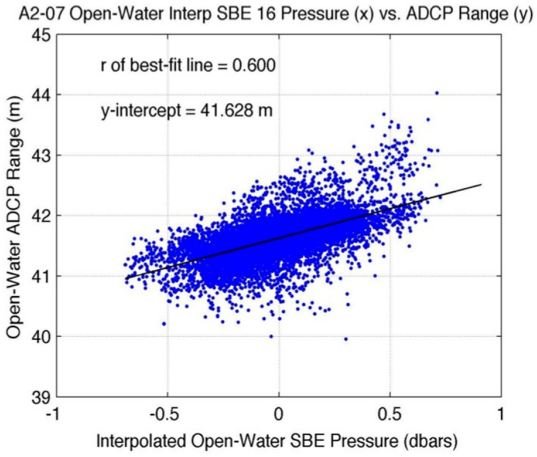

Figure 2.12: Scatterplot of interpolated SBE 16 pressure in db during open-water periods (x-axis) vs. corrected ADCP range in m during open-water periods (y-axis) at mooring A2-07. The y-intercept value represents the mean range of the ADCP to open water when the interpolated pressure variability is 0 db.

A secondary issue with the data at mooring A2-07 is that the temperature and salinity records from the SBE 16 are not complete for the full year of the mooring deployment. Therefore, to convert between pressure and depth, we use temperature and salinity data from the neighboring mooring A4W-07, located approximately 10 km to the east of A2-07. The density difference between these moorings is typically much less than 2 kg m^{-3} (Woodgate, 2004), and thus our use of the A4W-07 data at mooring A2-07 introduces a small (less than 0.2%) error. The resulting ADCP depth time series derived for A2-07 is shown in Figure 2.13.

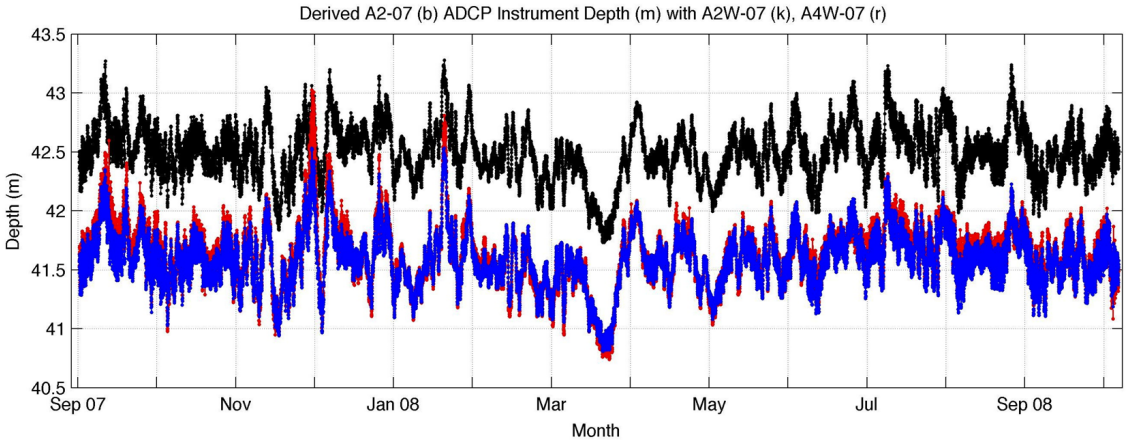

Figure 2.13: Derived ADCP depth time series for moorings A2W-07 (black), A4W-07 (red), and A2-07 (blue).

2.4.2.2.3 Quantifying Mooring Pull-Down with Bottom Pressure Gauge Data

An alternative strategy for inferring a pressure record at mooring A2-07 is to interpolate bottom pressure measurements across the strait and use a flow-derived estimate of mooring pull-down. To quantify the effects of mooring pull-down in the Bering Strait array, we use pressure data from the SBE 16 and BPG instruments at moorings A2W-07 and A4-07 (the two moorings with viable time series from both pressure sensors). From Equation (2.8), we first solve for the difference between BPG depth and SBE 16 depth, corrected for atmospheric effects. We determine the magnitude of M_3 using a process similar to that used to derive M_2, and subtract $(D_{\mathrm{B}} - D_{\mathrm{S}})$ from M_3 to obtain a time series of mooring pull-down (Figure 2.14(a), 2.14(b)).

Because pull-down results from flow drag on the mooring, we compare our pull-down time series to the ADCP-recorded water speed at bin 2 (measuring 6–8 m above the ADCP transducer head) (Figure 2.14(c), 2.14(d)). As illustrated in Figure 2.14, mooring pull-down effects are generally small at both moorings, typically less than about 0.2 m. The pull-down effect does not correlate strongly with current (Figure 2.14(e), 2.14(f)), although high flows appear related to the maximum observed pull-down at each mooring in late November–

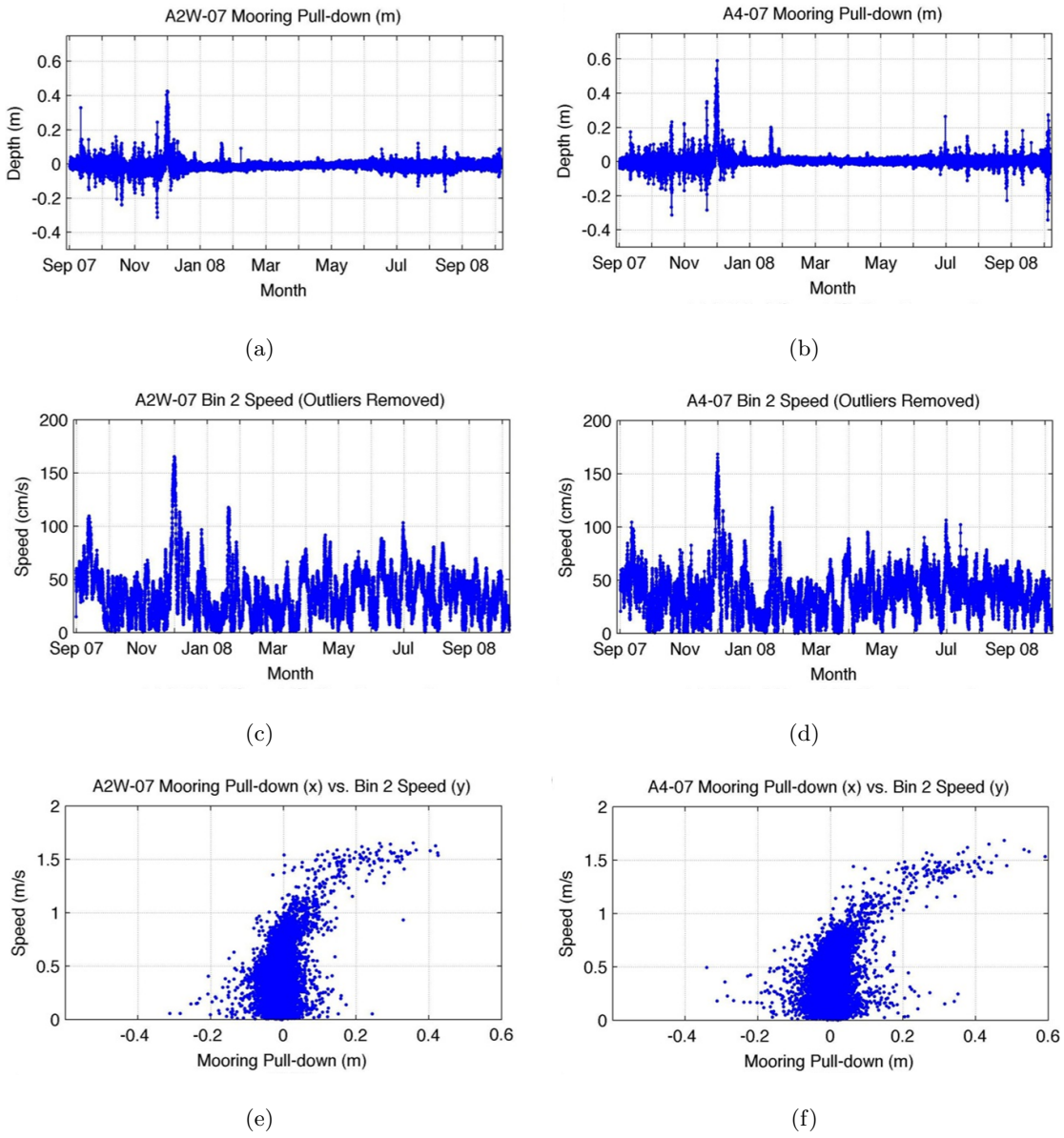

Figure 2.14: Plots of mooring pull-down time series at A2W-07 (a) and A4-07 (b), ADCP water-track speed time series from bin 2 for A2W-07 (c) and A4-07 (d), and scatterplots of mooring pull-down (x-axis) vs. bin 2 speed (y-axis) for A2W-07 (e) and A4-07 (f).

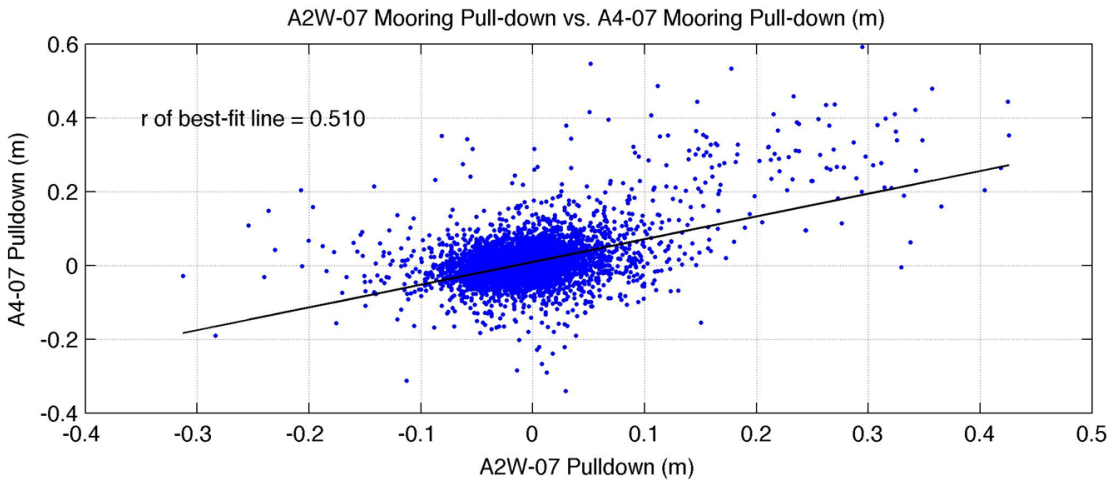

Figure 2.15: Scatterplot of mooring pull-down at A2W-07 (x-axis) vs. mooring pull-down at A4-07 (y-axis), with best-fit line and corresponding r value.

early December. The mooring pull-down signal is noisy (particularly in the inclusion of negative values), which could result from surface wave effects or a lack of synchronicity of the readings between the ADCP and the SBE 16. In comparing the pull-down time series at A2W-07 and A4-07 (Figure 2.15), we see a relatively low correlation, discouraging any further attempt to interpolate time series of pull-down for neighboring moorings.

2.4.2.2.4 Overall Error from ADCP Instrument Depth

To quantify the overall error associated with variations in ADCP instrument depth below the water surface, we take the standard deviation of the difference between the ADCP depth as inferred from ADCP range measurements and the ADCP depth inferred from SBE 16 pressure measurements. For the four eastern channel moorings, this value is of order 0.3 m, with a standard error about the record-length mean of order 0.05 m. While the uncertainty at A2-07 is likely greater due to our use of the interpolated pressure time series, the SBE 16 pressure sensors in the array are calibrated to be accurate to < 1 db. The BPG pressure sensors have a calibrated precision of ~ 0.006 db. Thus, the discrepancies

observed between derived instrument pressure and open-water range arise primarily due to inaccuracies in the ADCP ranges – indeed, the error we calculate is only slightly better than the manufacturer's estimated accuracy of 1% of the total range (i.e., ~ 0.4 m) (Teledyne RD Instruments, 2007). Thus, in the current application, use of more accurate pressure sensors would not have improved our estimates of ice thickness.

2.4.2.3 Sea-Ice Freeboard and Snow Loading

Just as current satellite systems cannot measure underwater sea-ice thickness, ADCPs offer no indication of ice and snow conditions above sea level. To quantify the total sea-ice volume flux through the Bering Strait, we need to consider both ice draft and ice freeboard, the latter of which is defined as the vertical distance between the air-snow or air-ice interface and the local sea surface ((Kwok and Cunningham, 2008)). For the purpose of this analysis, we consider the mass contributions of the sea-ice and snow components of ice freeboard separately.

We can derive a factor by which to estimate total sea-ice thickness from underwater ice thickness by applying Archimedes' Principle, which states that the upward force on an object floating in a fluid is equal to the weight of the fluid displaced by the object. Figure 2.16 illustrates a hypothetical piece of sea ice with which we estimate the relationship between sea-ice draft (D) and full ice thickness (T). We consider the underwater and above-sea-level sea ice separately due to differences in density of sea ice above and below the water (Timco and Frederking, 1996).

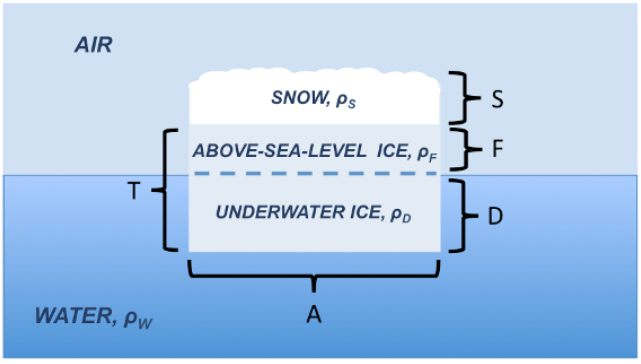

Variables:
D – Underwater Sea-Ice Thickness
F – Above-Sea-Level Sea-Ice Thickness
S – Snow Thickness
T – Total Ice Thickness

$\boldsymbol{\rho_D}$ – Density of Underwater Sea Ice
$\boldsymbol{\rho_F}$ – Density of Above-Sea-Level Sea Ice
$\boldsymbol{\rho_S}$ – Density of Snow
$\boldsymbol{\rho_W}$ – Density of Seawater
A – Horizontal Area of Sea Ice

Figure 2.16: Diagram of hypothetical piece of sea ice with snow contributing to height of sea-ice freeboard.

Using this figure, we can write the vertical force balance on the piece of sea ice as follows:

$$\rho_W DAg = \rho_D DAg + \rho_F FAg + \rho_S SAg \tag{2.11}$$

where A represents horizontal area, g is acceleration due to gravity, D, F, and S represent thicknesses of water/underwater ice, above-sea-level ice, and snow, respectively, and ρ represents density (with subscripts matching vertical thicknesses D, F, and S). We divide by Ag on both sides of the equation, and note that the total ice thickness we seek (T) is equal to $(F + D)$, thus obtaining:

$$\rho_W D = \rho_D D + \rho_F (T - D) + \rho_S S \tag{2.12}$$

We then solve for the total ice thickness, T, obtaining:

$$T = \frac{D(\rho_W - \rho_D + \rho_F)}{\rho_F} - \frac{S\rho_S}{\rho_F} \tag{2.13}$$

where D is the ice draft we calculate from the ADCP range data.

We use measured values and values from the literature (see Table 2.2) to estimate the various terms in Equation (2.13) for first-year sea ice. The range of water density values is determined from the monthly-averaged salinity values for January to April in the 1990–2004 Bering Strait climatology (Woodgate et al., 2005b).

Table 2.2: Representative Values of Snow, Ice, and Water Parameters

Variable	Estimated Value	Source of Estimate
Snow Thickness (S)	1–17 cm	Sturm et al. (2006)
Snow Density (ρ_S)	300 $\pm$ 100 kg m^{-3}	Warren et al. (1999)
Water Density (ρ_W)	1024.9–1027.4 kg m^{-3}	Woodgate et al. (2005b)
Underwater Ice Density (ρ_D)	900–940 kg m^{-3}	Timco and Frederking (1996)
Above-Sea-Level Ice Density (ρ_F)	840–910 kg m^{-3}	Timco and Frederking (1996)

By considering the extremes of these ranges, Equation (2.13) gives a range of values for T of $T = (1.09 \text{ to } 1.15)D + (0.002 \text{ to } 0.081)$. As the second term in this expression, representing snow loading on top of the sea ice, is small (only 8 cm) compared to our uncertainties in sea-ice draft, we discount the effects of snow loading in our assessment of ice freeboard. We thus determine full sea-ice thickness T to be 112 $\pm$ 3% of the ADCP-measured ice thickness, D. Note that the freshwater transport (rather than the ice volume transport) can be computed directly from the draft by making similar assumptions. We include the total ice volume here to allow for a better comparison to prior results.

2.5 Summary of Sea-Ice Thickness Corrections

Table 2.3 summarizes the instrument- and environment-based errors that we apply to extract sea-ice thickness from ADCP range data. In addition, the table provides estimated magnitudes of the manufacturer's range resolution error (1% of the range from the instrument to the surface, or $\sim$ 0.4 m for the Bering Strait array) (Teledyne RD Instruments, 2007), and the related error due to instrument pitch and roll (0.4 m) described by Woodgate and Holroyd (2011).

The errors marked with a star (*) in Table 2.3 originate from the same source (instrument

limitations), and it is reassuring that the various ways of assessing this uncertainty result in similar values. As we now combine all of the instrument- and environment-based errors to give a total error estimate, we need only include one estimate of the instrument limitation error. For our analysis, we use the beam averaging error of 0.35 m to represent the error due to instrument limitations of the ADCP. To estimate the total error remaining after corrections, we take the quadrature sum of the beam averaging error, beam footprint error, and ice freeboard and snow loading error, obtaining a total error value of order 0.5 m. Our estimate of total remaining error represents only a slight increase over the inherent range resolution error described by the instrument manufacturer. The remaining range error for the Bering Strait ADCPs is four times the magnitude of the error quoted by Melling et al. (1995) (0.1 m) in their IPS surveys of sea-ice thickness.

Table 2.3: Summary of Corrections for Sea-Ice Thickness. * Indicates errors that originate from the same source (which is considered only once in determining the estimated total error). For this analysis, the beam averaging error (0.35 m) is used to estimate total error.

Prior Information on ADCP Range Error Magnitude			
Reference	Description of Error	Estimated Magnitude of Error	Error Remaining After Correction
Teledyne RD Instruments (2007)	Instrument Range Resolution	0.4 m (1% of range to surface)	0.4 m*
Woodgate and Holroyd (2011)	Instrument Pitch and Roll	0–10 m	0.4 m*
Additional Range Errors Assessed in Bering Strait Mooring Array			
Error Description	Source of Error	Estimated Magnitude of Error	Error Remaining After Correction
Ridge-Shadowing	Instrument	Negligible for Bering Strait	Negligible
Beam Footprint	Instrument	Order 0.35 m (see Vinje et al., 1998)	Order 0.35 m
Beam Averaging	Instrument	0.35 m	0.35 m*
Sound Speed Variation	Environment	–0.02 m	Negligible
Instrument Depth Below the Sea Surface	Environment	0.3 m	0.3 m*
Ice Freeboard and Snow Loading	Environment	12 ± 3% of ice draft (for 1-m ice draft, 0.09–0.15 m; for 5-m ice draft, 0.45–0.75 m)	0.15 m
Estimated Total Error:			Order 0.5 m

Chapter 3

RESULTS AND DISCUSSION

In this chapter, we apply the errors described in Chapter 2 to generate a time series of ADCP-derived sea-ice thickness for each of the eastern channel moorings in the 2007 Bering Strait array. We then multiply our ice thickness time series by ADCP bottom-track velocity data to obtain a representation of sea-ice flux at each mooring site in the eastern channel. To quantify ice volume flux across the entire strait, we interpolate and extrapolate the mooring flux data across the full width of both the eastern and western channels. We assess the contribution of ice thickness variability to annual transport through the strait by calculating ice volume flux using a fixed ice thickness of 1 m, and comparing this to the estimates of flux made using the observed ice thicknesses. Finally, we compare our estimate of total annual sea-ice transport through the Bering Strait to previous estimates by Aagaard and Carmack (1989) and Woodgate and Aagaard (2005), and infer a corresponding volume of freshwater flux through the strait due to sea ice.

3.1 Sea-Ice Thickness Time Series

Figure 3.1 depicts the corrected ADCP sea-ice thickness time series (including sea-ice freeboard) for each of the four moorings in the eastern channel of the strait. Ice thickness statistics for each site, including mean and maximum thickness, are listed in Table 3.1. In comparing our ADCP-generated sea-ice thickness measurements to those estimated using the 2002 APL-ULS at mooring site A2 (not shown), we find our results to be of similar magnitude (Moritz, D., pers. comm.).

From the onset of sea-ice formation in mid-late December 2007, we see a gradual increase in sea-ice thickness from slight to 5–10 m (with occasional deeper keels) at all eastern channel

moorings through about mid-March. The greatest overall sea-ice thickness measurement of ~ 16 m was observed in late March at mooring A4-07 at one 30-min sample interval during a nine-hour period in which all measured ice thicknesses at the mooring were greater than 7 m. This mooring, located closest to the Alaskan coast, is likely to be affected by ridging of sea-ice against the coast (Figure 3.1(d)). As indicated in Table 3.1, the two moorings in the eastern channel closest to the Alaskan coast (A4W-07 and A4-07) experienced lower mean sea-ice thicknesses (although the means differ by less than our expected uncertainty in the range measurements) but greater isolated keel depths than the two moorings further west in the channel (A2W-07 and A2-07).

Interestingly, ADCP data from the easternmost two moorings in the channel (A4-07 and A4W-07) also suggest that in addition to having the thickest ice keels, there were more frequent ice-free periods there than at A2-07 and A2W-07. This could be due to leads forming near land-fast ice, although the ACC, which runs north along the coast of Alaska and continues to transport relatively fresh water through the strait in early winter (Woodgate and Aagaard, 2005), could contribute to this effect. Data from all four moorings indicate the presence of open-water in early to mid-May, signaling the seasonal break-up of the ice, but intermittent periods of sea-ice cover (generally 5 m or less) persist up until June.

Table 3.1: Ice Thickness Statistics for Eastern Channel ADCPs, Dec 2007–Jun 2008

Mooring (West to East)	Mean Sea-Ice Thickness (m)	Maximum Sea-Ice Thickness (m)
A2W-07	1.41	12.9
A2-07	1.47	11.7
A4W-07	1.31	14.5
A4-07	1.36	15.9

Figure 3.2 shows histograms of the corrected ADCP-derived full sea-ice thickness, divided into 10-cm bins, for the eastern channel moorings. The y-axis indicates the fraction of the

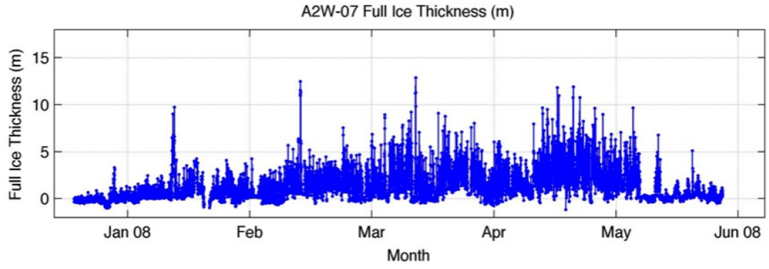

(a)

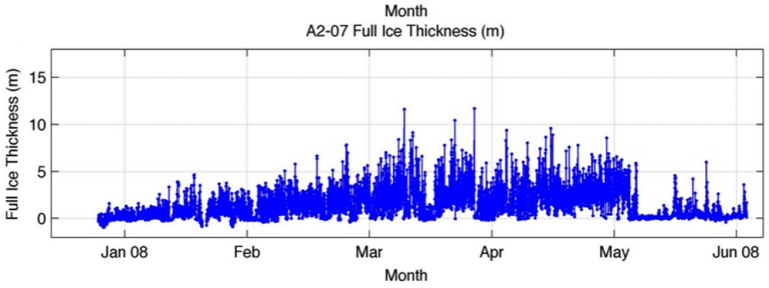

(b)

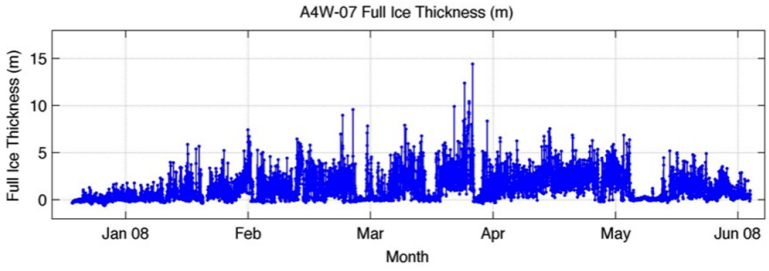

(c)

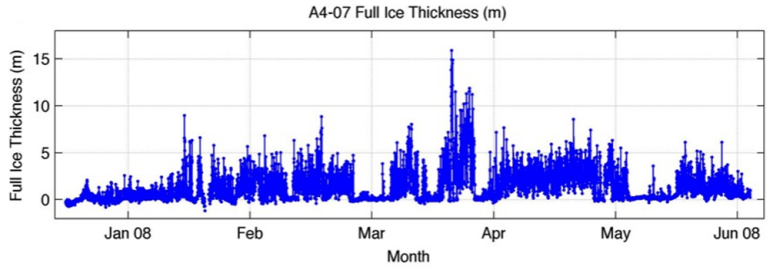

(d)

Figure 3.1: Corrected ADCP full sea-ice thickness time series for each of the four moorings A2W-07 (a), A2-07 (b), A4W-07 (c), and A4-07 (d) in the eastern channel of the Bering Strait.

total number of measurements at the mooring during the ice-covered period represented by each histogram bar. Negative values are suspected to result from sea surface heights greater than the open-water mean and/or mooring pull-down effects. For all moorings, we see the greatest concentration of ice thickness measurements are between 0 and 1 m. Note that these histograms cover the full season of observed ice presence in the Bering Strait, from mid-late December 2007 to early June 2008.

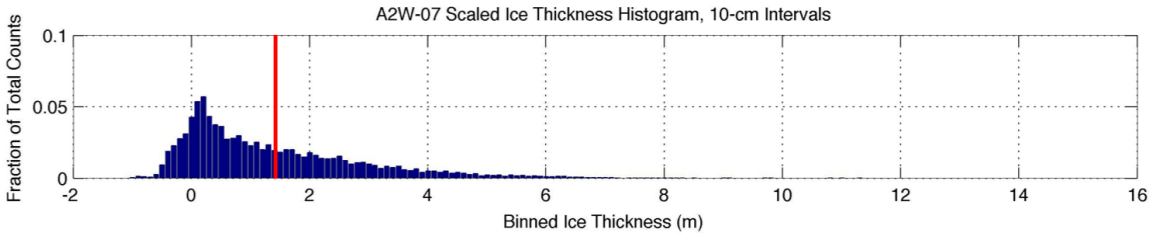

(a)

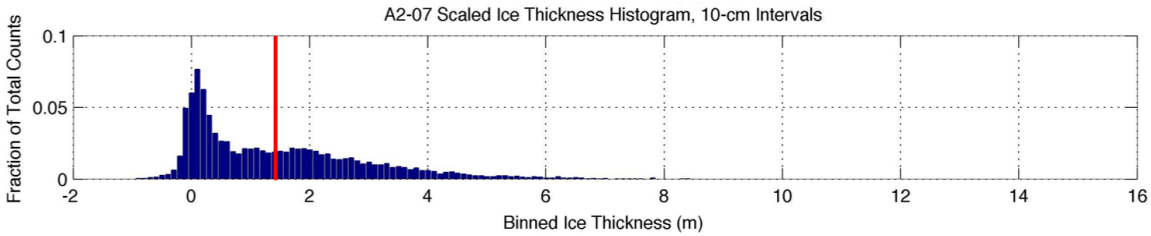

(b)

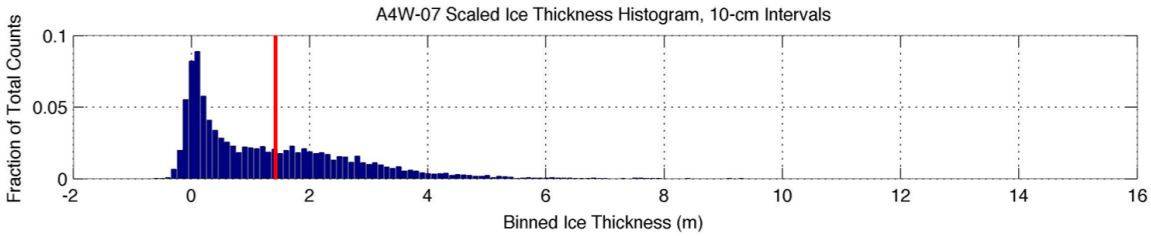

(c)

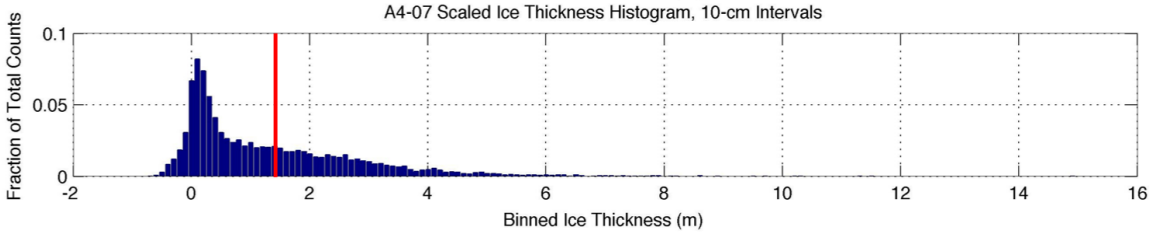

(d)

Figure 3.2: Histograms of corrected ADCP full sea-ice thickness data for each of the four moorings A2W-07 (a), A2-07 (b), A4W-07 (c), and A4-07 (d) in the eastern channel of the Bering Strait. The y-axis indicates the fraction of total measurements during ice-covered times at the mooring represented by each histogram bar. Red lines indicate the mean ice thickness of ~ 1.4 m observed across the eastern channel of the strait.

3.2 Along-Strait Sea-Ice Velocity

Estimating the volume of sea ice transiting the Bering Strait requires a time series of along-strait ice velocity. Although the ADCP water-track mode generates a binned velocity profile through the water column, data from the near-surface bins tend to be noisy (with high velocity errors). As a result, we use the ADCP bottom-track mode to obtain measurements of sea-ice velocity. The flow through the Bering Strait is predominantly unidirectional (north-south), and the same is true for the velocity of sea ice through the strait. In analyzing the principal component of bottom-track velocity data for the ADCPs moored in the eastern channel (A2W-07, A2-07, A4W-07, and A4-07), we find principal headings ranging from about 000°T to 008°T, explaining over 99% of the flow variance (Table 3.2). (All directions in this study have been corrected for magnetic declination.)

Table 3.2: Principal Component Analysis for Bering Strait Eastern Channel Moorings

Mooring (West to East)	Principal Heading (°T)	Frac. of Var. Explained
A2W-07	000°	0.991
A2-07	008°	0.982
A4W-07	006°	0.991
A4-07	006°	0.995

We seek to quantify sea-ice flux across the section of the Bering Strait where the line of moorings is located, and therefore need to measure the velocity component across this line. The mooring array is aligned from slightly northwest (277°T) to slightly southeast (097°T) across the strait. Thus, we seek velocities perpendicular to this section (i.e., along 007°T) and henceforth refer to this direction as "along-strait". Note that this heading is very close to the principal component headings, indicating that most of the ice flux is indeed across (and not along) the mooring section.

The along-strait ice velocities observed in the eastern channel using the ADCP bottom-track mode vary from about –125 to 200 cm s^{-1}, with positive velocities indicating flow in an

along-strait northward direction and negative velocities indicating along-strait southward flow. These velocities are close to the water-track velocity measurements, indicating that sea ice is (to first order) in free drift on the ocean. Older time series in the Bering Strait include periods when the ice velocity was recorded as zero despite a non-zero water velocity, suggesting the presence of land-fast ice above the mooring. No such events were recorded in the 2007–2008 Bering Strait mooring data.

3.3 Calculation of Sea-Ice Flux

To determine the sea-ice flux time series at each individual mooring site, we multiply the respective sea-ice thickness time series by the corresponding along-strait velocity data, and then interpolate this result across a designated width centered about the mooring site (hereafter referred to as a segment). Both ice thickness and velocity are recorded by the ADCPs every 30 min. To avoid spurious averaging effects, we calculate ice flux on the same half-hourly time base. In Figure 3.3, which shows data for the ice-covered period at mooring A4W-07, the seasonal break-up of sea ice coincides with higher and more variable velocity measurements (Figures 3.3(a), 3.3(b)). Predominant northward velocities persist during the intermittent return of sea ice in mid-late May, suggesting that the ice cover may result from advection of sea ice from the south. Similar results are observed at the other mooring sites, although the post break-up ice observed at moorings A2-07 and A2W-07 appears to be thinner overall than the ice observed at the easternmost moorings (Figure 3.1).

Given the errors described in Chapter 2 (Table 2.3), a complex interpolation scheme for sea-ice transport across the eastern channel of the Bering Strait is not justified. Instead, we use a very simple interpolation method, splitting the eastern channel section into four segments representing the following distances (from west to east):

- the Diomede Islands to the midpoint of A2W-07 and A2-07,
- the midpoint of A2W-07 and A2-07 to the midpoint of A2-07 and A4W-07,
- the midpoint of A2-07 and A4W-07 to the midpoint of A4W-07 and A4-07, and

– the midpoint of A4W-07 and A4-07 to the coast of Alaska.

We make the assumption that the ice thickness and ice velocity at each mooring are representative of the ice thickness and ice velocity across the segment in which the mooring falls. This is equivalent to linearly interpolating between the moorings (Figure 3.4). Subplot (c) of Figure 3.3 shows the sea-ice transport (in $m^3\ s^{-1}$) resulting from multiplying the two time series in Figure 3.3 (a) and (b) with the width of the segment centered about A4W-07 (Figure 3.4). In this resulting ice transport term, we see that increasing ice thickness in the Bering Strait modulates changes in flow velocity as winter progresses (Figure 3.3).

To examine the total transport variability of sea ice during periods of ice cover in the Bering Strait, we calculate cumulative ice transport over the winter season in m^3 (Figure 3.5). For each mooring, we determine cumulative transport across the respective segment using our ADCP-derived ice thickness time series (shown as a blue line), as well as the transport assuming a nominal ice thickness of one meter (result shown as a dashed red line). Comparing these two signals allows us to distinguish the effects of sea-ice thickness on ice volume flux from those due to variations in along-strait velocity. Negative ice transport values indicate southward transport through the strait, while positive values indicate northward transport. Until early to mid-April, the net ADCP-derived ice flux is to the south at all four moorings in the eastern channel of the Bering Strait (Figure 3.5). Taken over the entire winter, however, the annual sea-ice flux ranges from approximately 19 km^3 at A2W-07 to 31 km^3 at A4-07 northward.

By assuming a constant 1-m ice thickness, we incorrectly arrive at a net northward sea-ice flux starting earlier in the season (mid-late January in comparison to mid-April) at the three western moorings (A2W-07, A2-07, and A4W-07). (In our ADCP data, we observe that early northward flowing water carried little to no ice.) With the exception of a brief southward shift in cumulative transport during late March at mooring A4W-07, the net northward transport with 1-m ice thickness continues at these moorings into early June. At mooring A4-07, located closest to the Alaskan coast, the net transport with 1-m ice thickness does not shift northward until late January, and returns to southward transport

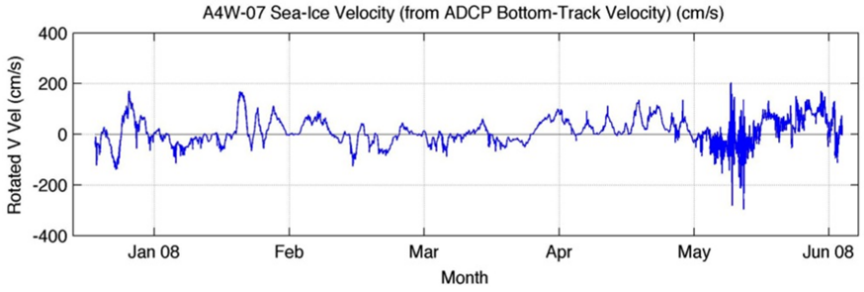

(a)

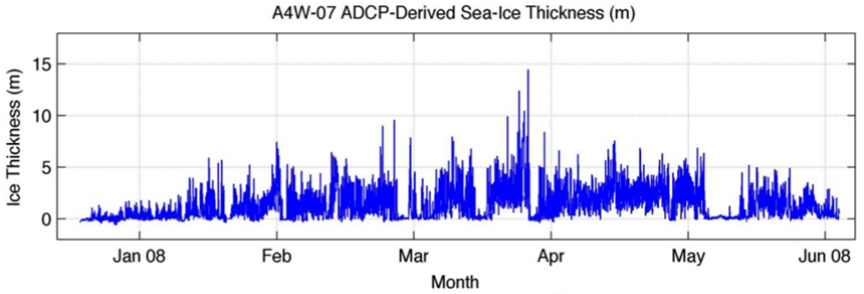

(b)

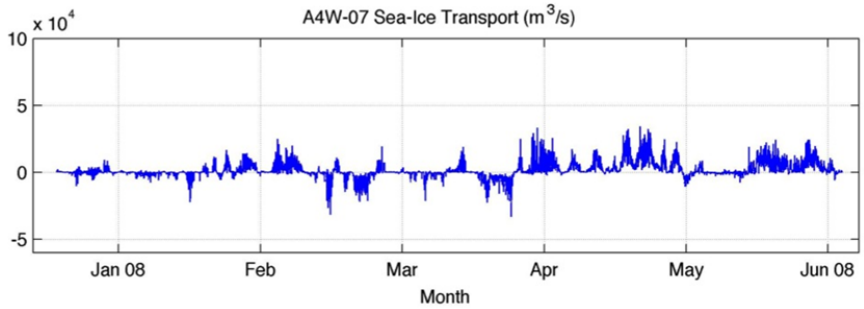

(c)

Figure 3.3: Mooring A4W-07 sea-ice velocity from ADCP bottom-track velocity data in cm s^{-1} (a), ADCP-derived sea-ice thickness in m (b), and overall transport of sea ice in m^3 s^{-1} (c).

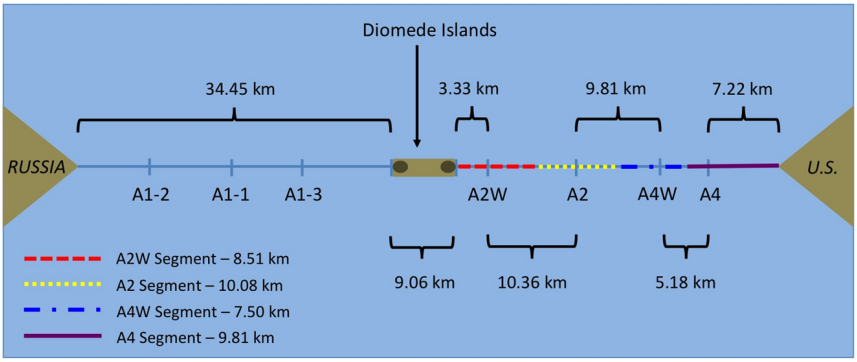

Figure 3.4: Cross-section of distances between Bering Strait moorings in the eastern channel and full distance across the western channel. The two Diomede Islands are treated as a connected landmass due to a lack of data for the channel that runs between the islands. Colored segments indicate the distances over which data from the respective moorings were interpolated.

by early March. Increasing the nominal ice thickness to 1.4 m (our approximate mean ice thickness across the eastern channel) results in final cumulative ice transport values that are closer to those calculated using ADCP-derived ice thicknesses at all four moorings. Such a change does not, however, significantly improve the ability of a constant-thickness time series to represent net transport variations over time. As a result, we conclude that a time series of sea-ice thickness data is needed to determine changes in ice transport over time, but that applying a nominal ice thickness value equal to the mean ice thickness of the time series will yield a reasonable estimate of the final net ice transport, if a reasonable mean ice thickness can be chosen.

Table 3.3 summarizes the transport of sea ice calculated for each segment in Figure 3.4 (listed by the mooring at the center of each segment across the eastern channel). Adding these, we find a total estimated transport through the eastern channel of the Bering Strait of 95 km^3 yr^{-1} with uncertainty of 35 km^3 yr^{-1}. We obtain this measure of uncertainty by considering the errors in our sea-ice thickness and velocity data, as well as the error we introduce by interpolating these data across the eastern channel. The error remaining in our ADCP ice thickness measurements (0.5 m) represents approximately 36% of the mean

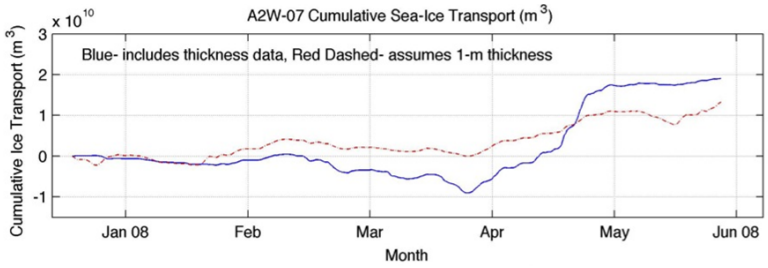

(a)

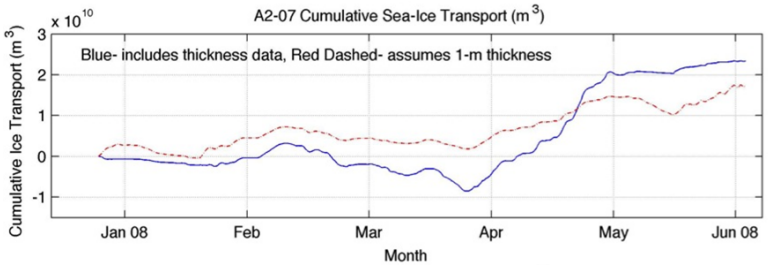

(b)

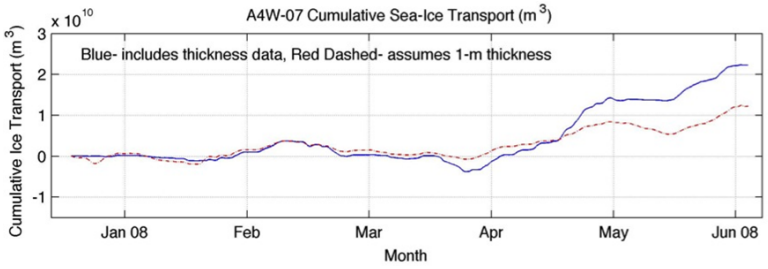

(c)

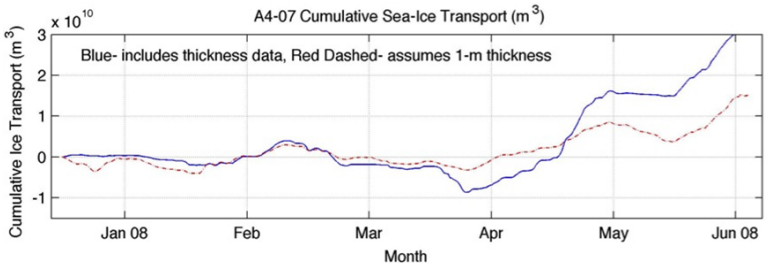

(d)

Figure 3.5: Cumulative sea-ice transport in km^3 from mid-December 2007 to June 2008 for moorings A2W-07 (a), A2-07 (b), A4W-07 (c), and A4-07 (d). In each subplot, the solid blue line represents sea-ice transport calculated using the ADCP-derived ice thickness data, while the dashed red line indicates ice transport calculated assuming a uniform ice thickness of 1 m.

Table 3.3: Summary of Sea-Ice Flux Statistics for Eastern Channel of Bering Strait from December 2007–June 2008

Mooring at Center of Segment	Segment Width (km)	Mean Ice Thickness (m)	Mean Ice Velocity (cm s^{-1})	Segment Transport (km^3 yr^{-1})	Transport per km (km^2 yr^{-1})	Fraction of Channel Transport
A4-07	9.81	1.4	10	31	3	0.32
A4W-07	7.49	1.3	11	22	3	0.23
A2-07	10.08	1.5	12	23	2	0.24
A2W-07	8.51	1.4	11	19	2	0.20
Total East Channel	35.89	1.4	11	96	3	1.00

Channel	Width (km)
Eastern	35.890
Western	36.445

ice thickness (1.4 m) at the eastern channel moorings. The error noted by the manufacturer in the ADCP velocity data (1 cm s^{-1}) represents approximately 9% of our mean sea-ice velocity (11 cm s^{-1})). Errors due to the interpolation across the eastern channel are more difficult to quantify, but we suspect them to be small due to the small variations in ADCP-derived mean ice thickness among the eastern channel moorings. We conclude that any interpolation errors are far smaller than the error due to sea-ice thickness, and neglect them in our calculation of sea-ice flux uncertainty. By adding the ice thickness and velocity error percentages in quadrature, we arrive at an uncertainty of 37% of the total sea-ice flux through the eastern channel.

As a note, the mean ice velocity values listed in Table 3.3 are averaged over positive (northward) and negative (southward) velocities; values in the table represent a mean northward velocity over the full ice-covered period. These mean ice velocities are less than the annual mean water velocity in the region since during ice-covered periods, southward winds typically prevail and slow the northward flow (Woodgate et al., 2005b,a).

3.4 Extrapolation of Sea-Ice Flux

As noted in Chapter 1, the sole ADCP deployed in the western channel of the Bering Strait at mooring A1-1-07 returned no viable data for 2007–2008. There is evidence to suggest that water flows in the eastern and western channels are highly correlated, and thus horizontal interpolation/extrapolation of along-strait velocity from mooring data is reasonable away from boundary currents (Woodgate et al., 2005a). As there is no ice information to the contrary, we make the simplest assumption and assume that western channel sea-ice flux has the same mean ice volume flux per km as the average of the eastern channel (approximately 3 km^3 yr^{-1} km^{-1}). This calculation is undoubtedly a simplification of sea-ice flux through the western Bering Strait, however without additional data, it represents our best estimate of ice transport west of the Diomede Islands (Table 3.4). As noted in Figure 3.4 above, we consider the two Diomede Islands to be a connected landmass, due to a lack of data for the 6-km wide channel that runs between the islands.

We estimate the sea-ice transport through the western channel of the Bering Strait to be 95 km^3 yr^{-1} with uncertainty of 35 km^3 yr^{-1} (calculated as described in Section 3.3). In Table 3.4, we include estimates of the western channel and total channel sea-ice flux calculated assuming that the ice-flux-per-km of the western channel matches the ice-flux-per-km of one of the eastern channel segments. This gives us a range of western channel ice fluxes of approximately 80–115 km^3 yr^{-1}, which we could use to estimate the additional error in our western channel ice flux estimate. The spread of these flux values (35 km^3 yr^{-1}) is similar to the uncertainty due to sea-ice thickness and velocity, suggesting that errors in our uncertainty due to across-strait interpolation are adequately represented by our overall error.

Combining the eastern and western channel cumulative sea-ice transports yields an estimated net sea-ice flux through the Bering Strait for the winter of 2007–2008 of 190 km^3 yr^{-1}, with uncertainty of 50 km^3 yr^{-1} (Table 3.4).

Table 3.4: Sea-Ice Flux Across Western Channel and Full Width of Bering Strait

Western Channel (Russia)

Flux Value Used for Estimate	Channel Transport (km^3 yr^{-1})
East Channel Avg	97
A4-07 Transport	114
A4W-07 Transport	108
A2-07 Transport	85
A2W-07 Transport	82

Full Strait (Eastern and Western Channels)

Flux Value Used for Estimate	Resulting Strait Transport (km^3 yr^{-1})
East Channel Avg	193
A4-07 Transport	210
A4W-07 Transport	204
A2-07 Transport	181
A2W-07 Transport	178

3.5 Comparison to Previous Sea-Ice Flux Estimates

To assess our estimates of sea-ice flux through the Bering Strait, we compare the total estimated sea-ice flux of 190 $\pm$ 50 km^3 yr^{-1} to previous estimates of ice transport through the strait. Aagaard and Carmack (1989) estimated the magnitude of sea ice through the Bering Strait into the Arctic to be about 30 km^3 yr^{-1}. Using moored instrumentation and ship-based observations, Woodgate and Aagaard (2005) estimated the sea-ice transport through the Bering Strait to be 130 $\pm$ 90 km^3 yr^{-1} for the winter of 1990–1991. While the 1990–1991 estimate does agree with our 2007–2008 estimate to within errors, it is informative to consider reasons why the two estimates would differ. One set of reasons is due to differences in methodology. The 1990–1991 ice transport estimate was calculated using a full-strait width of 75 km (Woodgate and Aagaard, 2005), a distance $\sim$ 12% shorter than the width of 85 km used in our analysis. Moreover, none of the pressure or range corrections discussed in this thesis were applied to the 1990–1991 data – as noted in Table 2.3, corrections due to effects such as instrument pitch and roll can be significant. The 1990–

1991 ice thickness and ice velocity data originated from a single moored ADCP deployed near the A2 site as opposed to a full mooring array (Woodgate and Aagaard, 2005). Although we have determined that transport values across the eastern channel of the Bering Strait are of similar magnitude for 2007–2008, there remain variabilities in ice transport across the strait that cannot be assessed using data from a single mooring. The second set of reasons for discrepancies between the 1990–1991 and 2007–2008 sea-ice flux time series is interannual change. While no intercomparison of ice thickness data between different years is available, there can be significant ($\sim 25\%$) variability in water volume transport from year to year in the strait (Woodgate et al., 2006).

3.6 Freshwater Flux

As described in Chapter 1, a third goal of this thesis is to compare the freshwater flux due to the sea ice transport we calculated to previous estimates of freshwater flux through the Bering Strait. Assuming a sea-ice salinity of 7 psu and using a reference salinity of 34.8 psu for the Arctic, Aagaard and Carmack (1989) estimated the freshwater transport due to sea ice through the Bering Strait to be 24 $km^3\ yr^{-1}$. This transport was determined to be a negligible contribution to their estimated 1670 $km^3\ yr^{-1}$ total freshwater flux through the strait (Aagaard and Carmack, 1989). Woodgate and Aagaard (2005) revisited this value after determining that the flux of sea ice through the Bering Strait was much greater than initially thought. Using the same sea-ice salinity of 7 psu, they estimated the freshwater contribution of sea ice through the Bering Strait to be $100 \pm 70\ km^3\ yr^{-1}$, or approximately 10% of the annual freshwater flux through the strait. This transport represented a significant change from the 24 $km^3\ yr^{-1}$ freshwater flux described by Aagaard and Carmack (1989), but an estimate with very substantial error bars (Woodgate and Aagaard, 2005).

To compare the contribution of our sea-ice volume transport to freshwater flow through the Bering Strait, we use the same reference and sea-ice salinities of 34.8 and 7 psu, respectively, as the previous studies. In addition, we use representative density values for ice, seawater, and freshwater of $\rho_{\mathrm{Ice}} = 920\ kg\ m^{-3}$, $\rho_{\mathrm{Sea}} = 1026\ kg\ m^{-3}$, and $\rho_{\mathrm{Fresh}} = 1000\ kg\ m^{-3}$. We

estimate the freshwater flux through the Bering Strait due to sea ice during the 2007–2008 ice season to be 140 ± 40 km^3 yr^{-1}, or 0.004 ± 0.001 Sv. This value agrees (within errors) with the freshwater flux due to sea ice of 100 ± 70 km^3 yr^{-1} determined by Woodgate and Aagaard (2005), but provides increased accuracy of the estimated flux.

Chapter 4

CONCLUSIONS

In this thesis, we used sea-ice thickness and ice velocity data from an array of subsurface moored ADCPs and other instruments to quantify sea-ice volume flux through the Bering Strait for 2007–2008, and to assess the utility of the Teledyne RD Instruments ADCP in measuring sea-ice thickness and thus, sea-ice flux.

To improve our estimates of sea-ice thickness from ADCP range data, we applied corrections to account for numerous instrument- and environment-based errors, which are summarized in Table 2.3. The predominant errors affecting our measurements result from instrument limitations, including ADCP pitch and roll effects (before correction up to 10 m, after correction $\sim$ 0.4 m), and smoothing of the range signal through beam averaging ($\sim$ 0.35 m). Other smaller errors that must still be considered in deriving sea-ice thickness are beam footprint error ($\sim$ 0.35 m) and the effects of ice freeboard and snow loading ($\sim$ 0.15 m). After making these corrections, we estimate that the ADCP can measure sea-ice thickness to an accuracy of order 0.5 m. For the Bering Strait winter of 2007–2008, our ADCP-derived sea-ice thickness measurements have a mean value of 1.4 m, with a maximum observed ice keel depth of nearly 16 m at mooring A4-07.

By multiplying the sea-ice thickness time series at each mooring by the ADCP-measured sea-ice velocity (uncertainty 1 cm s^{-1}) and respective across-strait segment width (Figure 3.4), we derived a series of sea-ice volume fluxes spanning the eastern channel of the strait. Through extrapolation, we derived a value of sea-ice flux for the western channel, which lacked the instrumentation to determine ice flux in situ. Combining the ice flux values for each channel, we estimated total sea-ice flux through the Bering Strait for the winter of 2007–2008 to be 190 km^3 yr^{-1}, with uncertainty of 50 km^3 yr^{-1}. Within errors, this agrees

with the sea-ice flux of 130 ± 90 km^3 yr^{-1} estimated by Woodgate and Aagaard (2005) using data from an ADCP deployed in the strait from 1990–1991, while simultaneously providing a significant reduction in uncertainty for our newer estimate. We do not necessarily expect agreement between these older and newer flux estimates, given that interannual variability in the strait is high, but the methods used by Woodgate and Aagaard (2005) did not include the numerous error corrections discussed in Chapter 2 of this thesis that make our newer estimate more accurate.

The freshwater flux through the strait that corresponds with our estimate of sea-ice flux is 140 ± 40 km^3 yr^{-1}, or 0.004 ± 0.001 Sv. This value also agrees (within errors) with the freshwater flux due to sea ice of 100 ± 70 km^3 yr^{-1} determined by Woodgate and Aagaard (2005), although again with increased accuracy. Our estimates represent a significant increase to the Bering Strait sea-ice freshwater flux estimate first suggested by Aagaard and Carmack (1989) of 24 km^3 yr^{-1}. In terms of contribution to the total freshwater flux through the strait (estimated at 2500 ± 300 km^3 yr^{-1}, (Woodgate and Aagaard, 2005)), even our current flux estimate of 140 km^3 yr^{-1} is small ($\sim$ 5%). However, the increased accuracy of our estimate will reduce the uncertainties in the estimate of total freshwater flux through the Bering Strait.

In addition to quantifying sea-ice and freshwater flux through the Bering Strait, a primary goal of our study was to evaluate the utility of moored upward-looking Teledyne RD Instruments ADCPs in estimating sea-ice draft. We determined the beam averaging error for our ADCPs to be approximately 0.35 m (close to the manufacturer's instrument range uncertainty of 0.4 m), and took this value to represent the error due to instrument limitations (Teledyne RD Instruments, 2007). By adding this error in quadrature to the beam footprint and ice freeboard/snow loading errors, we obtained the order 0.5-m error described above. With access to a more precise echo-sounding instrument (such as the Ice-Profiling Sonar (IPS) described by Melling et al. (1995), we might expect to reduce this overall range error. For example, Melling et al. (1995) suggest that the high-resolution IPS might have an instrument limitation error of 0.1 m (less than our value for the lower-resolution ADCP, as the IPS has better range estimation and only one sonar beam, and is therefore not affected by beam

averaging errors). Assuming that the footprint error and ice freeboard/snow loading errors remain as previously described, we estimate that using an IPS instead of an ADCP would yield a resulting range error of ~ 0.3 m, compared to our ADCP value of ~ 0.5 m. Thus, we expect that errors to ice-thickness measurements could be reduced somewhat (possibly by up to half) with the use of a more precise echo-sounding instrument to determine ice draft. However, the errors due to our interpolation of data across the strait are more difficult to quantify, and are likely to persist even if a more accurate sonar instrument is used. Thus, although an ADCP may not be the ideal tool if high-resolution ice keel surveys are required, the instrument proves effective at providing data to estimate sea-ice flux across a given line to a reasonable degree of accuracy (order 30%). Note that the ADCP fails to accurately record measurements of relatively thin sea ice as a result of the order 0.5-m ice thickness error described above.

As outlined in Chapter 1, satellite data provide excellent spatial coverage of sea-ice extent in the Arctic, however issues arise with coarse data resolution and the inability of satellites to directly measure full sea-ice thickness. Data from the Bering Strait mooring array provide the opportunity for ground-truthing of satellite ice presence and thickness data with an in situ source, although we do not explore this in our study. If the process of validating satellite data with in situ mooring data proves successful in the Bering Strait, the method may allow for similar ground-truthing of satellite sea-ice data elsewhere in the Arctic.

Finally, we consider the potential of historical ADCP records to provide estimates of past Bering Strait sea-ice fluxes. In addition to influencing the Arctic freshwater budget, variations in sea-ice flux through the strait affect the import of sediments and marine organisms in or on the sea ice. Quantifying changes in sea-ice flux over time is therefore crucial to understanding the effects of changing sea-ice extent and thickness on the Arctic ecosystem. In addition to the 2007–2008 time series, Bering Strait ADCP data for the longer period 2008–2011 presently await analysis, and could provide interesting information concerning interannual variability of sea-ice volume flux. Although year-round moorings have been deployed in the strait almost continuously since 1990, many of the earlier deployments consisted of a single mooring rather than a full array, and only in some years were ADCPs or

Upward Looking Sonars (ULSs) included in the array. As we noted in our earlier discussion of Woodgate and Aagaard (2005), interpolating data from a single instrument across a large distance can introduce additional errors to estimates of sea-ice characteristics. We are encouraged, however, by the similarity in our sea-ice flux-per-km measurements (Table 3.3), which indicate that at least for 2007–2008, the north-south transport of sea ice did not vary greatly across the strait. We are thus optimistic that similar methods to those used here could be applied to historical data to generate information on past sea-ice volume flux across the Bering Strait for use in modeling and predicting the fate of Arctic sea ice.

BIBLIOGRAPHY

Aagaard, K. and Carmack, E. C. (1989). The role of sea ice and other fresh water in the Arctic circulation. *Journal of Geophysical Research*, 94(C10):14485–14498.

Aagaard, K., Roach, A. T., and Schumacher, J. D. (1985). On the wind-driven variability of the flow through Bering Strait. *Journal of Geophysical Research*, 90(C4):7213–7221.

Aagaard, K. and Woodgate, R. A. (2001). Some thoughts on the freezing and melting of sea ice and their effects on the ocean. *Ocean Modelling 3*, pages 127–135.

Belliveau, D. J., Bugden, G. L., Eid, B. M., and Calnan, C. J. (1990). Sea ice velocity measurements by upward-looking Doppler current profilers. *Journal of Atmospheric and Oceanic Technology*, 7:596–602.

Bowditch, N. (2002). *The American Practical Navigator: An Epitome of Navigation*. National Imagery and Mapping Agency, Bethesda, MD, 2002 edition.

Chen, C.-T. and Millero, F. J. (1977). Speed of sound in seawater at high pressures. *Journal of the Acoustical Society of America*, 62(5):1129–1135.

Cherniawsky, J. Y., Crawford, W. R., Nikitin, O. P., and Carmack, E. C. (2005). Bering Strait transport from satellite altimetry. *Journal of Marine Research*, 63:887–900.

Coachman, L. K. and Aagaard, K. (1966). On the water exchange through Bering Strait. *Limnology and Oceanography*, 11(1):44–59.

Coachman, L. K., Aagaard, K., and Tripp, R. B. (1975). *Bering Strait: The Regional Physical Oceanography*. University of Washington Press, Seattle, WA.

Danielson, S., Curchitser, E., Hedstrom, K., Weingartner, T., and Stabeno, P. (2011). On

ocean and sea ice modes of variability in the Bering Sea. *Journal of Geophysical Research*, 116(C12034).

Drucker, R., Martin, S., and Moritz, R. (2003). Observations of ice thickness and frazil ice in the St. Lawrence Island polynya from satellite imagery, upward looking sonar, and salinity/temperature moorings. *Journal of Geophysical Research*, 108(C5):3149.

Gill, A. E. (1982). *Atmosphere-Ocean Dynamics*. Academic Press, San Diego, CA.

Huang, R. X. and Schmitt, R. W. (1993). The Goldsbrough-Stommel circulation of the world oceans. *Journal of Physical Oceanography*, 23:1277–1284.

Hyatt, J., Visbeck, M., Beardsley, R. C., and Owens, W. B. (2008). Estimating sea-ice coverage, draft, and velocity in Marguerite Bay (Antarctica) using a subsurface moored upward-looking acoustic Doppler current profiler (ADCP). *Deep-Sea Research II*, 55:351–364.

Jones, E. P., Swift, J. H., Anderson, L. G., Lipizer, M., Civitarese, G., Falkner, K. K., Kattner, G., and McLaughlin, F. (2003). Tracing Pacific water in the North Atlantic Ocean. *Journal of Geophysical Research*, 108(C4):3116.

Kovacs, A. (1996). Sea ice: Part I. Bulk salinity versus ice floe thickness. Technical Report CCREL Report 96-7, US Army Cold Regions Research and Engineering Laboratory.

Kwok, R. and Cunningham, G. F. (2008). ICESat over Arctic sea ice: Estimation of snow depth and ice thickness. *Journal of Geophysical Research*, 113(C08010).

Kwok, R., Cunningham, G. F., Manizade, S. S., and Krabill, W. B. (2012). Arctic sea ice freeboard from IceBridge acquisitions in 2009: Estimates and comparisons with ICESat. *Journal of Geophysical Research*, 117(C02018).

Kwok, R. and Rothrock, D. A. (2009). Decline in Arctic sea ice thickness from submarine and ICESat records: 1958-2008. *Geophysical Research Letters*, 36(L15501).

Laxon, S., Peacock, N., and Smith, D. (2003). High interannual variability of sea ice thickness in the Arctic region. *Nature*, 425:947–950.

Martin, T. (2007). *Arctic Sea Ice Dynamics: Drift and Ridging in Numerical Models and Observations*. University of Bremen, Bremen, Germany.

Maykut, G. A. (1985). An introduction to ice in the polar oceans. Technical Report APL-UW 8510, Applied Physics Laboratory, University of Washington., Seattle, WA.

Melling, H., Johnston, H., and Riedel, D. A. (1995). Measurements of the underside topography of sea ice by moored subsea sonar. *Journal of Atmospheric and Oceanic Technology*, 12:589–602.

National Snow and Ice Data Center (2012). Arctic ice extent low overall, high in the Bering Sea. *Arctic Sea Ice News & Analysis*.

RD Instruments (1998). *P/N 957-6000-00, Workhorse Acoustic Doppler Current Profiler Technical Manual*. Poway, CA.

Roach, A. T., Aagaard, K., Pease, C. H., Salo, S. A., Weingartner, T., Pavlov, V., and Kulakov, M. (1995). Direct measurements of transport and water properties through the Bering Strait. *Journal of Geophysical Research*, 100(C9):18443–18457.

Serreze, M. C., Barrett, A. P., Slater, A. G., Woodgate, R. A., Aagaard, K., Lammers, R. B., Steele, M., Moritz, R., Meredith, M., and Lee, C. M. (2006). The large-scale freshwater cycle of the Arctic. *Journal of Geophysical Research*, 111(C11010).

Serreze, M. C., Holland, M. M., and Stroeve, J. (2007). Perspectives on the Arctic's shrinking sea-ice cover. *Science*, 315:1533–1536.

Shcherbina, A. Y., Rudnick, D. L., and Talley, L. D. (2005). Ice-draft profiling from bottom-mounted ADCP data. *Journal of Atmospheric and Oceanic Technology*, 22:1249–1266.

Spreen, G., Kaleschke, L., and Heygster, G. (2008). Sea ice remote sensing using AMSR-E 89-GHz channels. *Journal of Geophysical Research*, 113(C02S03).

Steele, M., Morison, J., Ermold, W., Rigor, I., and Ortmeyer, M. (2004). Circulation of summer Pacific halocline water in the Arctic Ocean. *Journal of Geophysical Research*, 109(C02027).

Sturm, M., Maslanik, J. A., Perovich, D. K., Stroeve, J. C., Richter-Menge, J., Markus, T., Holmgren, J., Heinrichs, J. F., and Tape, K. (2006). Snow depth and ice thickness measurements from the Beaufort and Chukchi Seas collected during the AMSR-Ice03 campaign. *IEEE Transactions on Geoscience and Remote Sensing*, 44(11):3009–3020.

Teledyne RD Instruments (2007). *P/N 957-6156-00, WorkHorse Commands and Output Data Format*. Poway, CA.

Teledyne RD Instruments (2011). *P/N 951-6069-00, Acoustic Doppler Current Profiler Principles of Operation A Practical Primer*. Poway, CA.

Timco, G. W. and Frederking, R. M. W. (1996). A review of sea ice density. *Cold Regions Science and Technology*, 24:1–6.

Torgerson, L. J. and Stringer, W. J. (1985). Observations of double arch formation in the Bering Strait. *Geophysical Research Letters*, 12(10):677–680.

Vinje, T., Nordlund, N., and Kvambekk, A. (1998). Monitoring ice thickness in Fram Strait. *Journal of Geophysical Research*, 103(C5):10437–10449.

Visbeck, M. and Fischer, J. (1995). Sea surface conditions remotely sensed by upward-looking ADCPs. *Journal of Atmospheric and Oceanic Technology*, 12:141–149.

Wadhams, P. (1978). Characteristics of deep pressure ridges in the Arctic Ocean. In *Proc. 4th Intl. Conf. Port and Ocean Engng. under Arctic Conditions (POAC '77)*, Memorial University, St. John's, Newfoundland.

Wadhams, P. (1981). Sea-ice topography of the Arctic Ocean in the region 70 degrees W to 25 degrees E. *Philosophical Transactions of the Royal Society A*, 302:45–85.

Wadley, M. R. and Bigg, G. R. (2002). Impact of flow through the Canadian Archipelago and Bering Strait on the North Atlantic and Arctic circulation: An ocean modelling study. *Quarterly Journal of the Royal Meteorological Society*, 128:2187–2203.

Walsh, J., McRoy, C., Coachman, L., Goering, J., Nihoul, J., Whitledge, T., Blackburn, T., Parker, P., Wirick, C., and Shuert, P. (1989). Carbon and nitrogren cycling within the

Bering/Chukchi Seas: Source regions for organic matter effecting AOU demands of the Arctic Ocean. *Progress in Oceanography*, 22(4):277–359.

Warren, S. G., Rigor, I. G., Untersteiner, N., Radionov, V. F., Bryazgin, N. N., Aleksandrov, Y. I., and Colony, R. (1999). Snow depth on Arctic sea ice. *Journal of Climate*, 12:1814–1829.

Weingartner, T. J., Danielson, S., Sasaki, Y., Pavlov, V., and Kulakov, M. (1999). The Siberian Coastal Current: A wind- and buoyancy-forced Arctic coastal current. *Journal of Geophysical Research*, 104(C12):29697–29713.

Woodgate, R. A. (2004). Alpha Helix HX290 cruise report, Bering Strait mooring cruise August–September 2004. Cruise report, University of Washington. http://psc.apl.washington.edu/BeringStrait.html.

Woodgate, R. A. and Aagaard, K. (2005). Revising the Bering Strait freshwater flux into the Arctic Ocean. *Geophysical Research Letters*, 32(2).

Woodgate, R. A., Aagaard, K., and Weingartner, T. J. (2005a). A year in the physical oceanography of the Chukchi Sea: Moored measurements from autumn 1990–1991. *Deep-Sea Research Part II: Topical Studies in Oceanography*, 52(24–26):3116–3149.

Woodgate, R. A., Aagaard, K., and Weingartner, T. J. (2005b). Monthly temperature, salinity, and transport variability of the Bering Strait throughflow. *Geophys. Res. Lett.*, 32(L04601).

Woodgate, R. A., Aagaard, K., and Weingartner, T. J. (2006). Interannual changes in the Bering Strait fluxes of volume, heat and freshwater between 1991 and 2004. *Geophysical Research Letters*, 33(L15609).

Woodgate, R. A., Aagaard, K., and Weingartner, T. J. (2007). First steps in calibrating the Bering Strait throughflow: Preliminary study of how measurements at a proposed climate site (A3) compare to measurements within the two channels of the strait (A1 and A2). Technical report, University of Washington.

Woodgate, R. A., Crane, K., Zhdanov, M., Wood, K., Smolin, V., and Whitledge, T. (2008). Mooring cruise report for RUSALCA SEVER cruise to the Bering Strait - Aug/Sept 2007. Cruise report, University of Washington., Seattle, WA. http://psc.apl.washington.edu/BeringStrait.html.

Woodgate, R. A. and Holroyd, A. E. (2011). Correction of Teledyne Acoustic Doppler Current Profiler (ADCP) bottom-track range measurements for instrument pitch and roll. Technical report, University of Washington., Seattle, WA.

Woodgate, R. A., Weingartner, T., and Lindsay, R. (2010). The 2007 Bering Strait oceanic heat flux and anomalous Arctic sea-ice retreat. *Geophysical Research Letters*, 37(L01602).